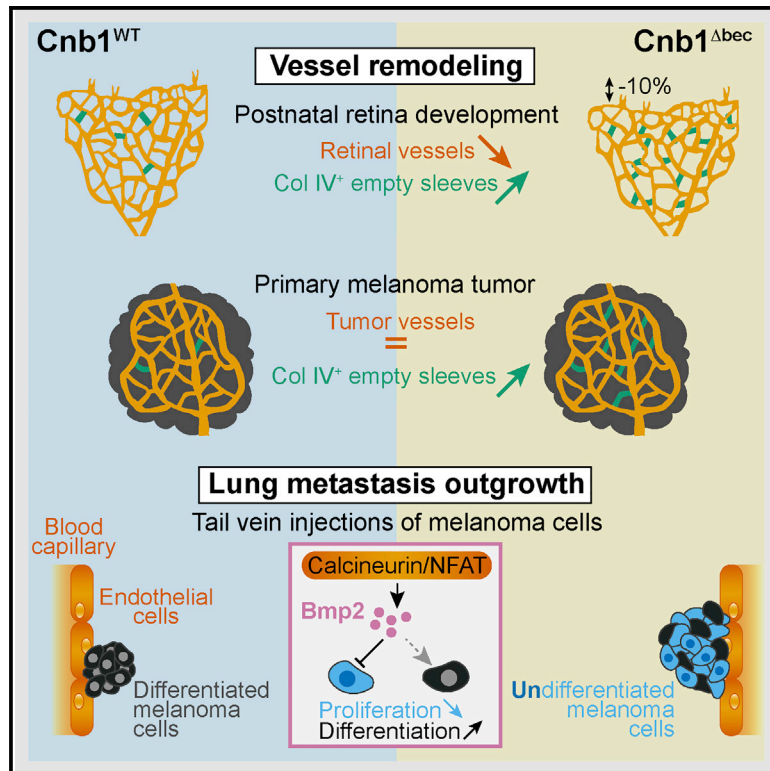# Cell Reports

Endothelial Calcineurin Signaling Restrains Metastatic Outgrowth by Regulating Bmp2

Graphical Abstract

Authors

Stefanie Hendrikx, Sanja Coso, Borja Prat-Luri, ..., Holger Gerhardt, Mauro Delorenzi, Tatiana V. Petrova

Correspondence

tatiana.petrova@unil.ch

In Brief

Hendrikx et al. show that endothelial calcineurin signaling is dispensable for physiological and tumor angiogenesis. Instead, it promotes vascular stabilization and, in cancer, restrains metastatic outgrowth. Immunosuppressive therapy with calcineurin inhibitors thus also directly affects the endothelium, which may contribute to aggressive cancer progression in organ transplant recipients.

Highlights

- Endothelial calcineurin is dispensable for physiological and tumor angiogenesis

- Endothelial calcineurin stabilizes vessels and restrains metastatic outgrowth

- Calcineurin/NFAT target BMP2 induces differentiation of metastatic cells

CellPress

Article

Endothelial Calcineurin Signaling Restrains Metastatic Outgrowth by Regulating Bmp2

Stefanie Hendrikx,[1,2,3] Sanja Coso,[1,2,3,10,11] Borja Prat-Luri,[1,2,3,10] Laureline Wetterwald,[1,2,3] Amélie Sabine,[1,2,3]
Claudio A. Franco,[4] Sina Nassiri,[5,6] Nadine Zangger,[5,6] Holger Gerhardt,[7,8] Mauro Delorenzi,[2,5,6]
and Tatiana V. Petrova[1,2,3,9,12,*]
[1]Department of Oncology, University of Lausanne, Lausanne 1011, Switzerland
[2]Ludwig Institute for Cancer Research Lausanne, Lausanne, Switzerland
[3]Division of Experimental Pathology, CHUV, Epalinges 1066, Switzerland
[4]Instituto de Medicina Molecular - João Lobo Antunes, Faculdade de Medicina, Universidade de Lisboa, Lisbon, Portugal
[5]Bioinformatics Core Facility, SIB Swiss Institute of Bioinformatics, Lausanne 1015, Switzerland
[6]Translational Bioinformatics and Statistics, Swiss Cancer Center Lausanne, Department of Oncology, University of Lausanne,
Lausanne 1011, Switzerland
[7]Vascular Patterning Laboratory, Department of Oncology, KU Leuven, Leuven, Belgium
[8]Integrative Vascular Biology Laboratory, Max-Delbrück-Center for Molecular Medicine (MDC) in the Helmholtz Association, Berlin Institute of
Health (BIH), German Center for Cardiovascular Research (DZHK) Partner Site, Berlin, Germany
[9]Swiss Institute for Cancer Research, École Polytechnique Fédérale de Lausanne, Lausanne 1015, Switzerland
[10]These authors contributed equally
[11]Present address: Moores Cancer Center, University of California, San Diego, La Jolla, CA 92093, USA
[12]Lead Contact
*Correspondence: tatiana.petrova@unil.ch
https://doi.org/10.1016/j.celrep.2019.01.016

SUMMARY

Calcineurin/NFAT signaling is active in endothelial cells and is proposed to be an essential component of the tumor angiogenic response. Here, we investigated the role of endothelial calcineurin signaling *in vivo* in physiological and pathological angiogenesis and tumor metastasis. We show that this pathway is dispensable for retinal and tumor angiogenesis, but it is implicated in vessel stabilization. While ablation of endothelial calcineurin does not affect the progression of primary tumors or tumor cell extravasation, it does potentiate the outgrowth of lung metastases. We identify Bmp2 as a downstream target of the calcineurin/NFAT pathway in lung endothelium, potently inhibiting cancer cell growth by stimulating differentiation. We reveal a dual role of calcineurin/NFAT signaling in vascular regression or stabilization and in the tissue-specific production of an angiocrine factor restraining cancer cell outgrowth. Our results suggest that, besides targeting the immune system, post-transplantation immunosuppressive therapy with calcineurin inhibitors directly targets the endothelium, contributing to aggressive cancer progression.

INTRODUCTION

The formation of new blood vessels, or angiogenesis, is a hallmark of many human cancers that supports tumor growth and metastasis (De Palma et al., 2017). Signaling via vascular endothelial growth factors (VEGFs) and their endothelial receptor tyrosine kinases (VEGFRs) are essential for vessel growth and remodeling. Blocking VEGF-A/VEGFR-2 interaction or downstream signaling pathways such as phosphoinositide 3-kinase (PI3K), the mammalian target of rapamycin (mTOR), and Akt interfere with angiogenesis and vascular maintenance in many pathological and physiological situations (De Palma et al., 2017; Graupera et al., 2008; Kerr et al., 2016). VEGFR-2 activation also triggers the Ca^{2+}/phospholipase-C gamma cascade, which activates the Ca^{2+}-dependent serine/threonine phosphatase calcineurin. Calcineurin dephosphorylates the nuclear factor of activated T cells (NFAT), leading to its nuclear entry and transcriptional activity. Among the 5 members of the NFAT family, NFAT1–NFAT4 are regulated by calcineurin. They were first described in T cells; however, it is now evident that they are expressed by numerous cell types and have a wide range of cellular functions (Mancini and Toker, 2009).

In vitro studies of the calcineurin/NFAT pathway suggested that it is a key downstream mediator of VEGFA-VEGFR2 responses, such as endothelial cell (EC) migration and proliferation (Minami et al., 2004; Schweighofer et al., 2009; Zaichuk et al., 2004). However, the *in vivo* role of the calcineurin/NFAT signaling pathway in the tumor vasculature is not fully understood. Studies of Down syndrome critical region-1 (DSCR1), a direct target and endogenous inhibitor of calcineurin/NFAT, showed that Dscr1 overexpression suppresses calcineurin signaling, inhibits tumor angiogenesis, and prevents tumor growth (Baek et al., 2009). Dscr1 germline deletion reduced tumor growth as a result of overactive calcineurin signaling, leading to EC apoptosis (Ryeom et al., 2008). In addition, $Dscr1^{-/-}$ mice develop more lung metastases due to the increased production of angiopoietin-2, which promotes vascular permeability and facilitates tumor cell extravasation (Minami et al., 2013).

Here, we directly investigated the role of calcineurin signaling in tumor angiogenesis, growth, and metastasis, using a model with
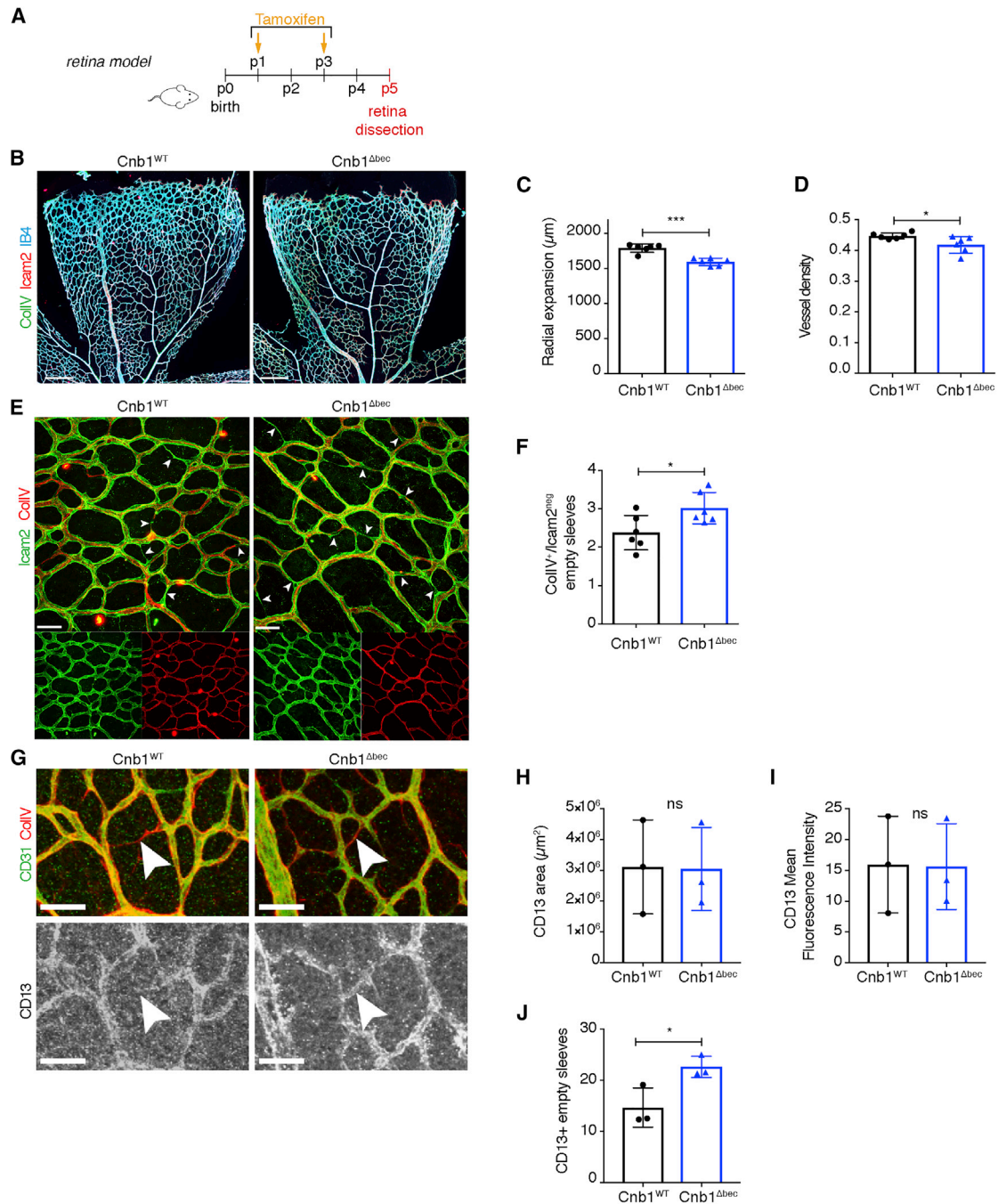
Figure 1. Endothelial Calcineurin Signaling Controls Vessel Regression in the Postnatal Retina

(A) Scheme for tamoxifen injection and retina collection of pups.

(B) Representative images of a retina leaflet from Cnb1^{WT} and Cnb1$^{\Delta bec}$ pups. Staining for collagen IV (green), Icam2 (red), and IB4 (blue).

(C) Vascular radial expansion is impaired in Cnb1$^{\Delta bec}$ retinas. ***p = 0.0001; n = 6 Cnb1^{WT}; n = 6 Cnb1$^{\Delta bec}$.

(D) Vessel density measured by IB4 is reduced in Cnb1$^{\Delta bec}$ retinas. *p = 0.0347; n = 6 Cnb1^{WT}; n = 6 Cnb1$^{\Delta bec}$.

(E) Representative images of empty sleeves from Cnb1^{WT} and Cnb1$^{\Delta bec}$ retinas. Staining for Icam2 (green) and collagen IV (red). Arrowheads indicate empty sleeves.

(F) The number of empty sleeves is increased in Cnb1$^{\Delta bec}$ retinas. Quantification of the number of Icam2^{-}, collagen IV^{+} area normalized to the total vascularized area. *p = 0. 0273; n = 6 Cnb1^{WT}; n = 6 Cnb1$^{\Delta bec}$.

(G) Increased association of pericytes with empty collagen sleeves in Cnb1$^{\Delta bec}$ retina. Immunofluorescent staining for pericyte marker CD13 (gray), CD31 (green), and collagen IV (red). Arrowheads indicate a CD13^{-} empty sleeve in Cnb1^{WT} and a CD13^{+} empty sleeve in Cnb1$^{\Delta bec}$.

(H) Quantification of total pericyte coverage in Cnb1^{WT} and Cnb1$^{\Delta bec}$ pups. n = 3 Cnb1^{WT}; n = 3 Cnb1$^{\Delta bec}$.

inducible endothelial-specific ablation of calcineurin. In contrast to previous observations *in vitro* and in *Dscr1* transgenic and knockout mice, we observed that calcineurin is dispensable for both physiological and pathological angiogenesis, but it contributes to vessel stabilization. Such decreased vascular stability does not significantly affect primary tumor growth; however, loss of endothelial calcineurin stimulates the outgrowth of lung metastases by decreasing bone morphogenetic protein-2 (Bmp2) production, thereby reducing cancer cell differentiation. Our data reveal a dual role of calcineurin/NFAT signaling in the vasculature: a general role as a fine-tuner of vessel stabilization and an organ-specific role as a regulator of a paracrine factor that restrains metastasis outgrowth. They also indicate that besides targeting the immune system, post-transplantation immunosuppressive therapy with calcineurin inhibitors directly targets the endothelium, thereby contributing to aggressive cancer progression.

RESULTS

Endothelial Calcineurin Signaling Regulates Vessel Regression in the Postnatal Retina

We investigated the role of calcineurin in physiological angiogenesis using the mouse postnatal retina model (Gerhardt et al., 2003). Analysis of P5 retinas from mice with endothelial-specific inactivation of the main calcineurin subunit Cnb1 (Cnb1$^{\Delta bec}$) or wild-type (Cnb1^{WT}) (Figure 1A) demonstrated that Cnb1$^{\Delta bec}$ retinal vascularization was decreased, as shown by a reduced radial expansion and vessel density (Figures 1B–1D). However, the loss of endothelial calcineurin had no impact on the apoptosis and proliferation of ECs, as determined by staining for caspase-3 and 5-ethynyl-2′-deoxyuridine (EdU) incorporation (Figures S1A and S1B). No changes were observed in the morphological appearance of the angiogenic front (Figure S1C) or in arterial or venous branching from the main vessels (Figures S1D and S1E) in Cnb1^{WT} and Cnb1$^{\Delta bec}$ retinas.

We next analyzed whether the loss of calcineurin affects vessel stabilization. Vessel maturation is characterized by an increased deposition of basement membrane, pericyte recruitment, and pruning of the excessive blood vasculature (Fruttiger, 2007; Korn and Augustin, 2015). Vessel regression is induced by low-flow conditions to which ECs respond by retracting and undergoing apoptosis or by migrating away and integrating elsewhere in the vascular tree (Franco et al., 2015; Korn and Augustin, 2015). In doing so, ECs leave behind collagen IV$^+$ "empty sleeves" (Baluk et al., 2003). The number of empty sleeves was increased in Cnb1$^{\Delta bec}$ retina; however, there was no change in the overall pericyte coverage, as determined by staining for the pericyte marker CD13 (Armulik et al., 2011) (Figures 1E–1H). Higher numbers of pericytes remained associated with the empty sleeves of Cnb1$^{\Delta bec}$ retinas (Figures 1G, 1I, and 1J), indicating that such pericytes may survive better or migrate less after the retraction of calcineurin-deficient ECs. Our data indicate that

calcineurin signaling does not contribute to sprouting angiogenesis, but rather is implicated in vessel stabilization.

Endothelial Calcineurin Signaling Is Dispensable for Tumor Angiogenesis and Tumor Growth

To study the role of calcineurin in pathological angiogenesis, we injected syngeneic melanoma B16F10 cells subcutaneously in Cnb1^{WT} and Cnb1$^{\Delta bec}$ mice (Figure 2A). The growth of primary B16F10 tumors was minimally decreased in Cnb1$^{\Delta bec}$ animals, and we observed similar results in the Lewis lung carcinoma model (Figure 2B and data not shown). The quantification of tumor volume over time and tumor weight after sacrifice showed a non-significant tendency toward reduced primary tumor size in Cnb1$^{\Delta bec}$ mice (Figures 2C and 2D). EGFP was uniformly high in tumor ECs, indicating high activity of the *Pdgfb*-iCreERT2-Ires-EGFP transgene (Claxton et al., 2008), and analysis of sorted tumor ECs confirmed the significantly reduced expression of both *Cnb1* and the calcineurin/NFAT target gene *Dscr1* (Figures S2A–S2C). Further analysis of the tumor vasculature did not reveal differences in vascular density or vessel pericyte coverage between Cnb1^{WT} and Cnb1$^{\Delta bec}$ tumors (Figures 2E–2H), indicating that calcineurin is dispensable for tumor vessel expansion and maturation.

The loss of calcineurin increased the number of empty sleeves in the retinal vasculature (Figure 1F); therefore, we analyzed collagen IV distribution in B16F10 tumors. We observed no change in the overall collagen IV staining (Figures 2I and 2J). However, when analyzing the avascular collagen IV, we noticed an increase in the collagen IV$^+$ empty sleeves in Cnb1$^{\Delta bec}$ tumors (Figures 2I and 2K). Our results indicate that similar to the retinal vasculature, calcineurin is dispensable for the tumor angiogenic response but fine-tunes the tumor vessel stability, and its inactivation has only a marginal impact on primary tumor growth.

Calcineurin Deletion in the Endothelium Increases Cancer Cell Metastasis in the Lung

To study the role of endothelial calcineurin in a metastatic context, we injected intravenously (i.v.) B16F10 cells (Figure 3A). We analyzed whether the early steps of metastasis are affected, and 5 days after the i.v. injection, there was no detectable difference in the number of lung metastases between Cnb1^{WT} and Cnb1$^{\Delta bec}$ mice (Figures 3B and 3C). However, we observed significantly more metastases in Cnb1$^{\Delta bec}$ lungs compared to wild-type lungs 12 days after cancer cell injection (Figures 3D and 3E). The increased metastasis in Cnb1$^{\Delta bec}$ lungs was also apparent at 19 days post-injection (Figures 3F and 3G), but the difference between the 2 genotypes was less prominent. Similarly, i.v.-injected MC38-GFP colorectal cancer cells generated significantly more metastases in Cnb1$^{\Delta bec}$ mice (Figures S3A and S3B). Our results thus indicate that endothelial calcineurin signaling restrains the growth of lung metastasis.

(I) CD13 mean fluorescence intensity (MFI) is similar between Cnb1^{WT} and Cnb1$^{\Delta bec}$ pups. n = 3 Cnb1^{WT}; n = 3 Cnb1$^{\Delta bec}$.

(J) Cnb1$^{\Delta bec}$ retinas have an increased number of CD13$^+$ pericytes in the empty sleeves area. *p = 0.0346; n = 3 Cnb1^{WT}; n = 3 Cnb1$^{\Delta bec}$.

ns, not significant; error bars represent means ± SDs. Two-tailed Student's t test was performed on all of the data represented.

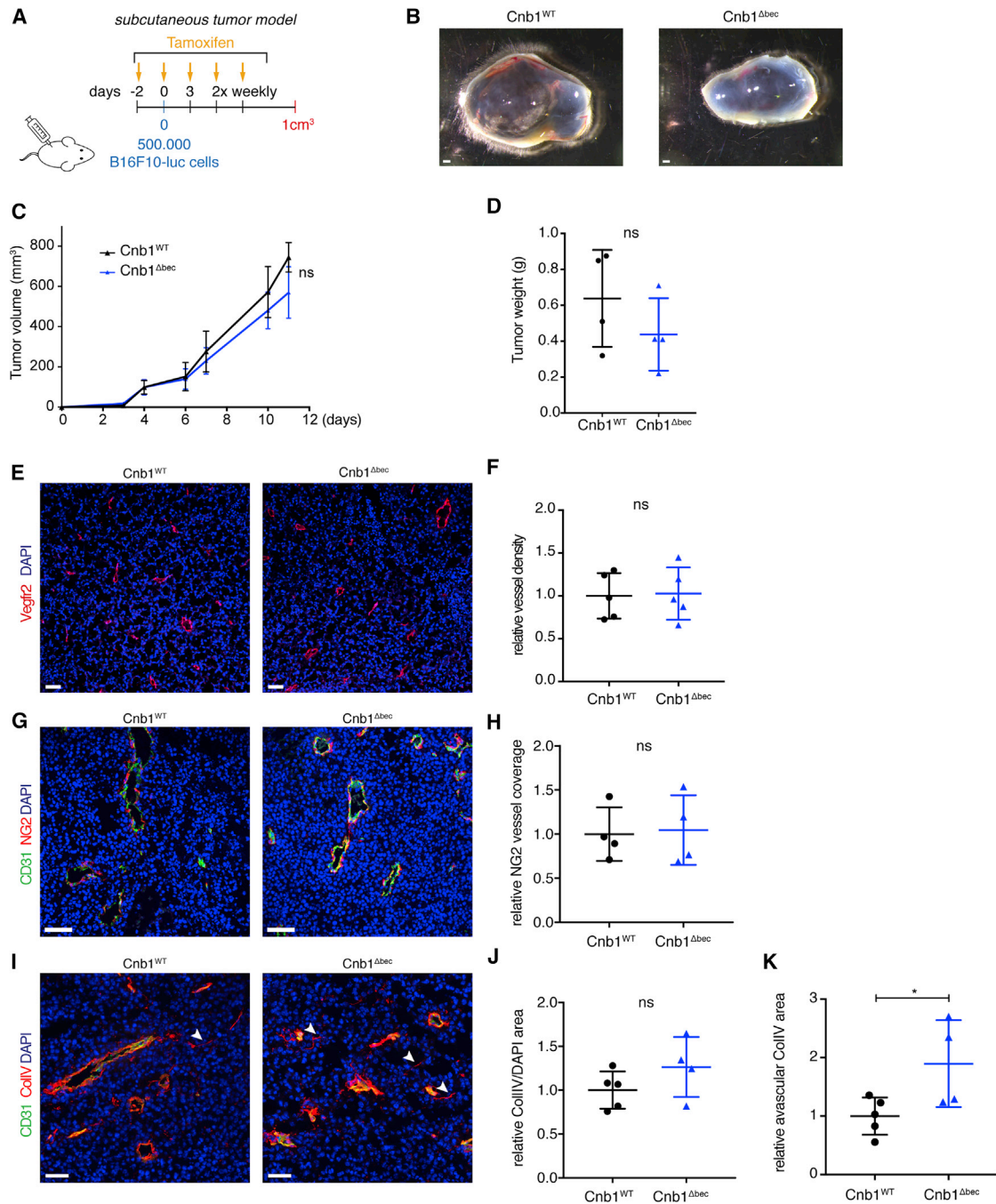Scale bars: (B) 200 μm, (E and G) 50 μm.

Figure 2. Endothelial Calcineurin Signaling Does Not Affect Primary Tumor Growth and Angiogenesis

(A) Scheme for tamoxifen and subcutaneous B16F10-luc cell injections.

(B) Representative pictures of tumors *ex vivo* from Cnb1^{WT} and Cnb1$^{\Delta bec}$ mice.

(C) Tumor growth is not affected in Cnb1$^{\Delta bec}$ mice; n = 4 per genotype.

(D) Tumor weight is not affected in Cnb1$^{\Delta bec}$ mice; n = 4 per genotype.

(E) Comparable primary tumor blood vascular density in Cnb1^{WT} and Cnb1$^{\Delta bec}$ mice. Staining for Vegfr2 (red) and DNA (blue) of primary tumors.

(F) Quantification of the blood vessel density in Cnb1^{WT} and Cnb1$^{\Delta bec}$ tumors. Vegfr2 area was normalized to the total DAPI area and plotted relative to wild-type (WT); n = 5 per genotype.

(G) Representative images of pericytes in Cnb1^{WT} and Cnb1$^{\Delta bec}$ B16F10 primary tumors. Staining for NG2 (red), CD31 (green), and DNA (blue).

(H) Pericyte (NG2) area normalized to the CD31 area is comparable in Cnb1^{WT} and Cnb1$^{\Delta bec}$ tumors; n = 4 per genotype.

(I) More avascular collagen IV is present in Cnb1^{WT} tumors compared to Cnb1$^{\Delta bec}$ tumors. Immunofluorescent staining for collagen IV (red) and CD31 (green) in Cnb1^{WT} and Cnb1$^{\Delta bec}$ tumors. Arrowheads indicate empty sleeves.

(legend continued on next page)

Immune cells are major players in metastasis initiation and progression. Natural killer (NK) cells and Cd8$^+$ T cells can eradicate metastatic cancer cells, whereas macrophages and neutrophils enhance metastasis formation (Kitamura et al., 2015). Therefore, we analyzed major immune cell populations in Cnb1^{WT} and Cnb1$^{\Delta bec}$ lungs after i.v. injection of B16F10 cells. We did not observe significant changes in B cells, neutrophils, monocytes and macrophages, or NK cells between Cnb1^{WT} and Cnb1$^{\Delta bec}$ mice. Although there was some increase in naive T cell infiltration in Cnb1$^{\Delta bec}$ animals, this did not translate into significant changes in activated and memory T cells (Figures S4A–S4G). Thus, the increased metastasis phenotype observed in Cnb1$^{\Delta bec}$ mice is likely not initiated by immune cells.

Calcineurin Deletion in the Endothelium Increases the Outgrowth Potential of Cancer Cells in Lungs

To evaluate whether calcineurin affects the survival of cancer cells in the circulation or their extravasation, we analyzed the fate of fluorescently labeled B16F10 cells in the lungs 24 h after i.v. injection. A similar number of cancer cells were present in the lungs of wild-type and Cnb1$^{\Delta bec}$ mice (Figures S4H and S4I). Thus, endothelial calcineurin/NFAT signaling does not play a major role in early metastatic dissemination.

To study whether this pathway affects the outgrowth of cancer cells in the lung microenvironment, we injected Cnb1^{WT} and Cnb1$^{\Delta bec}$ mice i.v. with B16F10 cells first and deleted calcineurin 5 days later (Figure 4A), when micrometastases were already established. Mice were sacrificed 12 days after tumor cell injection, and thus 7 days after calcineurin inactivation. As expected, there was no difference in the total number of metastatic foci between Cnb1^{WT} and Cnb1$^{\Delta bec}$. However, we observed a significantly increased number of large colonies (>0.5 mm) in Cnb1$^{\Delta bec}$ lungs compared to Cnb1^{WT} lungs (Figures 4B–4D), indicating that endothelial calcineurin restrains metastatic outgrowth.

The largest difference in metastatic foci was observed at day 12 (Figures 3D and 3E), but it was reduced at a later stage (Figures 3F and 3G). These results suggest that calcineurin is important during the initial metastatic outgrowth, but contributes less after metastatic lesions have reached a certain size. To study this question, we induced calcineurin deletion 9 days after the i.v. injection of cancer cells (Figure 4E), and the metastases were quantified at day 16. In this setting, we did not observe changes in the number or size of the metastatic foci between Cnb1^{WT} and Cnb1$^{\Delta bec}$ mice (Figures 4F–4H). We thus conclude that the endothelium of Cnb1$^{\Delta bec}$ mice promotes the outgrowth of cancer cells during a restricted period.

The increased outgrowth at early stages could be due to the fact that in macrometastases, proportionally fewer tumor cells are located in the vicinity of blood vessels (Figure S5A). The growth of cancer cells in macrometastases thus may be less

sensitive to the endothelial-derived paracrine factors. We evaluated whether calcineurin loss affects the proliferation of cancer cells in macrometastases by analyzing EdU incorporation. We did not observe any differences in the proliferation of cancer cells in macroscopic lesions of Cnb1^{WT} or Cnb1$^{\Delta bec}$ lungs when analyzing lungs 19 days post-injection of cancer cells (Figures S5B and S5C). However, in the 12-day outgrowth experiments, we observed an increase in the EdU$^+$ metastatic area in Cnb1$^{\Delta bec}$ lungs compared to wild-type lungs (Figures 5A and 5B). Further analysis using GFP-labeled B16F10 cells confirmed the increased proliferation of cancer cells 12 days post-injection in Cnb1$^{\Delta\Delta bec}$ lungs (Figures 5C and 5D). We also evaluated whether endothelial NFAT signaling is influenced by the presence of metastasis and whether such activation is organ specific. The expression of the direct NFAT target gene Dscr1 was not affected in the lung endothelium by the presence of cancer cells (Figure S5D). However, we observed that the basal level of NFAT signaling in the lung ECs was significantly higher in comparison to ECs from the gut and skin (Figure S5E). Our data thus reveal tissue-specific differences in the levels of endothelial calcineurin activation and show that its loss promotes the proliferation of lung micrometastases.

Calcineurin Signaling Regulates Bmp2 Expression in Lung Endothelial Cells

To mechanistically unravel the contribution of endothelial calcineurin signaling to cancer cell outgrowth, we transduced human umbilical vein ECs (HUVECs) with lentiviruses encoding a constitutively active form of NFATc1 (caNFATc1). The mutation of serines in the SRR and SPXX repeat motifs of the NFATc1 regulatory domain prevents the phosphorylation of NFATc1 and imposes its nuclear localization (Monticelli and Rao, 2002). As expected, HUVECs transduced with caNFATc1 had increased nuclear NFATc1 levels compared to GFP controls (Figures S6A and S6B). Similarly, a lower-motility NFATc1 band was observed in lysates from caNFATc1-HUVECs, confirming the loss of phosphorylation (Figure S6C). There was a 10-fold upregulation of the NFAT target DSCR1 in caNFATc1-HUVECs, thereby confirming the overactivation of NFAT signaling (Figure 6A). To identify potential paracrine factors that affect metastatic outgrowth, we analyzed the expression of cell surface or secreted molecules that were previously shown to be regulated in HUVECs by calcineurin/NFAT (Suehiro et al., 2014; Figure S6D). We observed a significantly increased expression of Tissue Factor and BMP2, but not of other target genes such as VCAM1, ANG2, or ESELECTIN or another member of the BMP family, BMP4 (Figure 6A).

To study whether the target genes identified by our in vitro analyses are also regulated by calcineurin signaling in vivo, we sorted lung blood ECs from wild-type and Cnb1$^{\Delta bec}$ mice i.v. injected with B16F10 cells (Figures S6E–S6H). As expected, we observed a strong decrease in Cnb1 in ECs from Cnb1$^{\Delta bec}$

(J) Overall collagen IV staining in Cnb1^{WT} and Cnb1$^{\Delta bec}$ tumors is unchanged; n = 5 Cnb1^{WT}; n = 4 Cnb1$^{\Delta bec}$.

(K) Avascular collagen IV is increased in Cnb1$^{\Delta bec}$ tumors compared to WT tumors. Quantification of the avascular (CD31$^-$) collagen IV area or empty sleeves, plotted relative to WT. *p = 0.0399; n = 5 Cnb1^{WT}; n = 4 Cnb1$^{\Delta bec}$.

ns, not significant; error bars represent means ± SDs. Two-tailed Student's t test was performed on all of the data represented.
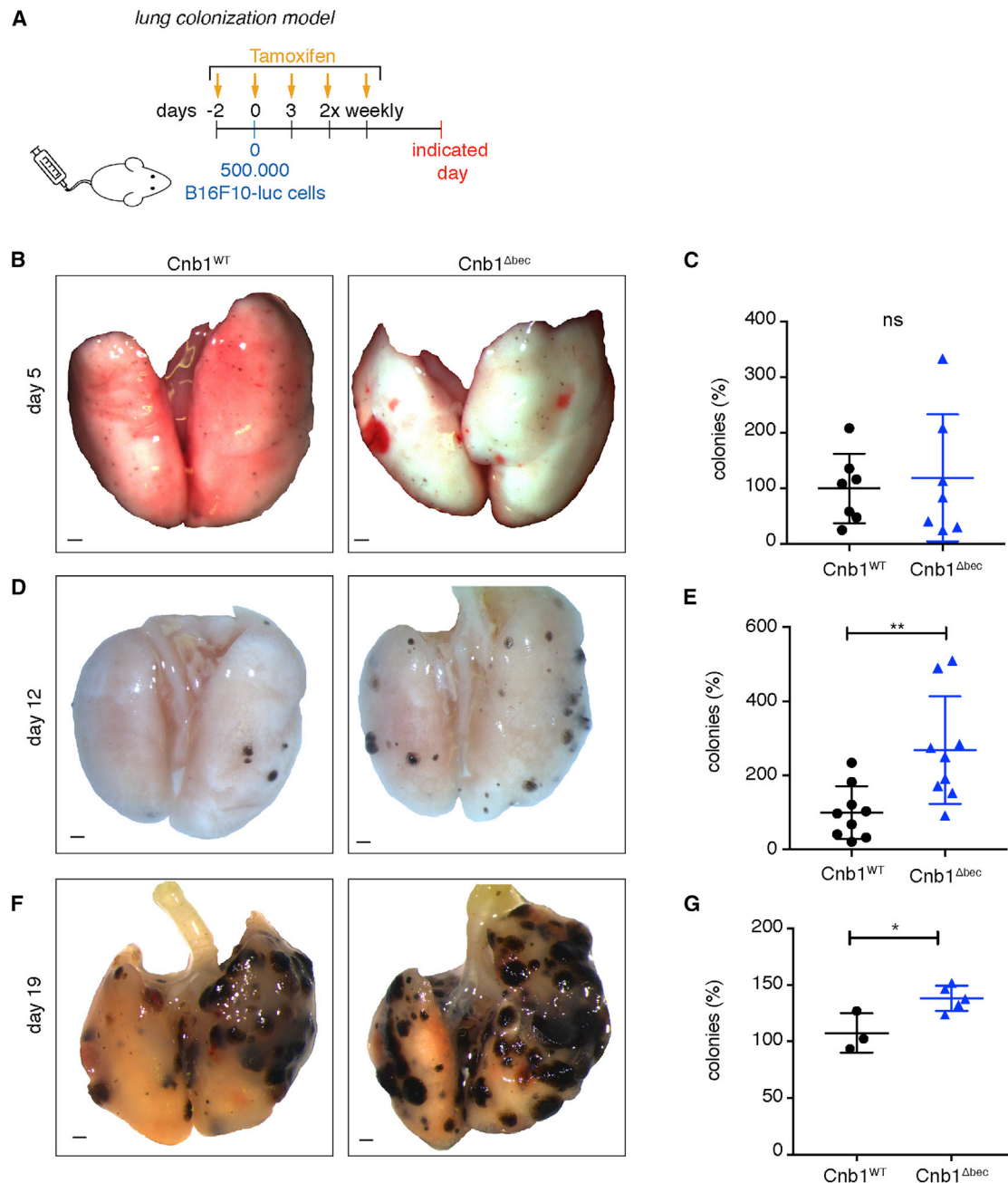
Scale bars: (B) 1 mm, (E) 50 μm, (G and I) 100 μm.

Figure 3. Endothelial Calcineurin Signaling Restrains Lung Metastasis

(A) Scheme for tamoxifen and B16F10 cell injections.

(B) Representative images of lungs 5 days after B16F10 i.v. injection.

(C) The number of B16F10 colonies in lungs is not affected in Cnb1$^{\Delta bec}$ mice 5 days after i.v. injection; n = 7 per genotype. Data combined from 2 independent experiments.

(D) Representative images of lungs 12 days after B16F10 i.v. injection.

(E) Cnb1$^{\Delta bec}$ lungs have more B16F10 colonies 12 days after tumor cell injection. **p = 0.0066; n = 9 per genotype. Data combined from 2 independent experiments.

(F) Representative images of Cnb1$^{\Delta bec}$ and Cnb1^{WT} lungs 19 days after B16F10 i.v. injection.

(G) Cnb1$^{\Delta bec}$ lungs have more B16F10 colonies 19 days after tumor cell injection. *p = 0.0212; n = 3 Cnb1^{WT}; n = 5 Cnb1$^{\Delta bec}$.

ns, not significant; error bars represent means ± SDs. Two-tailed Student's t test was performed on all of the data represented.
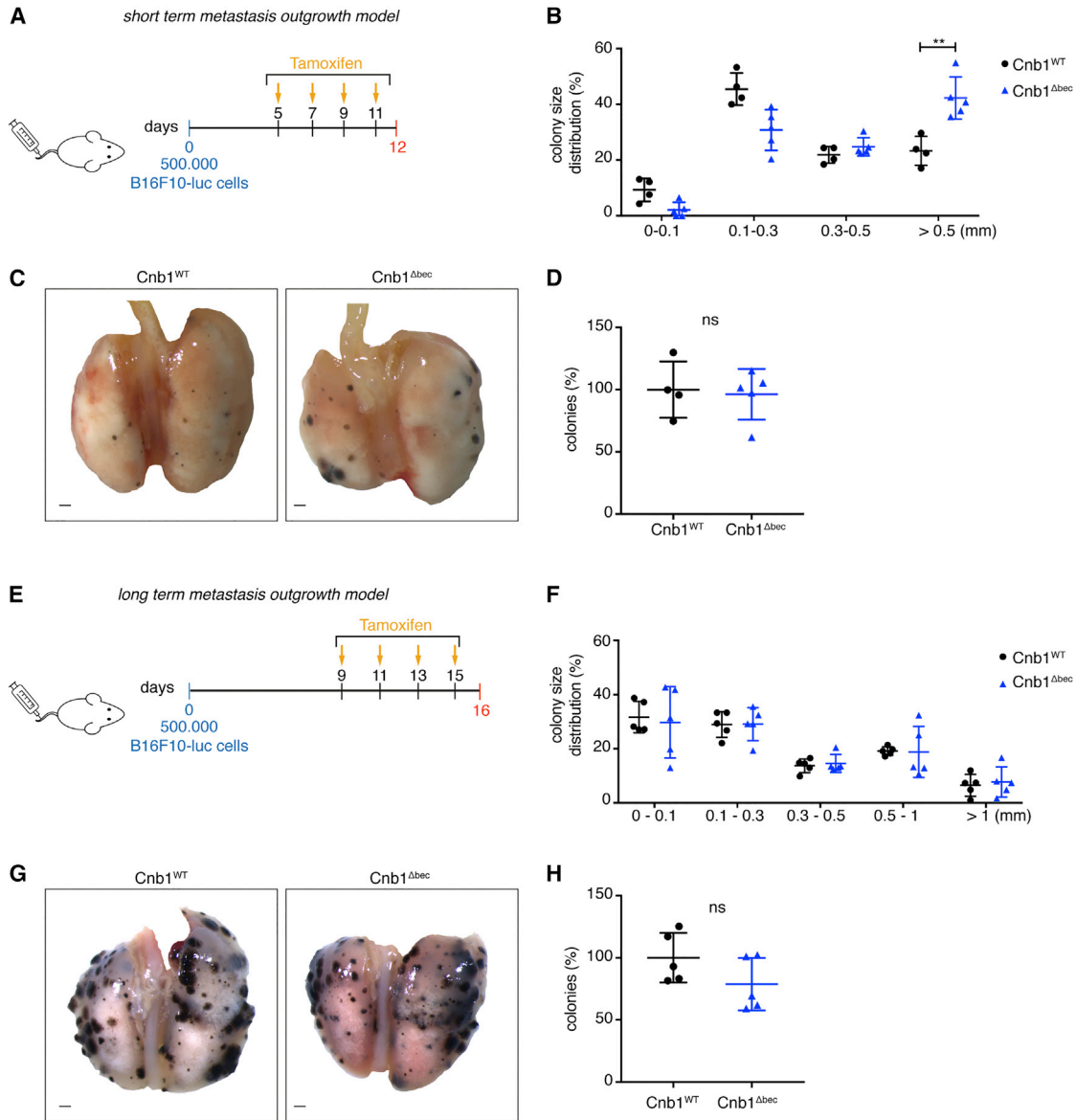
Scale bars: (B, D, and F) 1 mm.

Figure 4. Endothelial Calcineurin Deletion Increases the Outgrowth of Metastatic Cancer Cells

(A) Scheme for tamoxifen and intravenous (i.v.) B16F10 injection for early outgrowth experiments.

(B) Cnb1$^{\Delta bec}$ lungs have significantly larger (>0.5 mm) colonies compared to Cnb1^{WT} lungs 12 days after i.v. injection and tamoxifen administration at day 5. **p = 0.0037; n = 4 Cnb1^{WT}; n = 5 Cnb1$^{\Delta bec}$.

(C) Representative pictures of lungs from Cnb1^{WT} and Cnb1$^{\Delta bec}$ mice from the 12-day outgrowth experiment.

(D) The number of lung B16F10 colonies is not affected in Cnb1$^{\Delta bec}$ mice 12 days after i.v. injection and tamoxifen administration at day 5; n = 4 Cnb1^{WT}; n = 5 Cnb1$^{\Delta bec}$.

(E) Scheme for tamoxifen and intravenous B16F10 injections for late outgrowth experiments.

(F) Similar size B16F10 colonies are present in Cnb1^{WT} and Cnb1$^{\Delta bec}$ lungs 16 days after i.v. injection and tamoxifen administration at day 9; n = 5 Cnb1^{WT}; n = 4 Cnb1$^{\Delta bec}$.

(G) Representative pictures of Cnb1^{WT} and Cnb1$^{\Delta bec}$ lungs from the 16-day outgrowth experiment.

(H) The number of lung B16F10 colonies is not affected in Cnb1$^{\Delta bec}$ mice 16 days after i.v. injection and tamoxifen administration at day 9; n = 5 Cnb1^{WT}; n = 4 Cnb1$^{\Delta bec}$.

ns, not significant; error bars represent means ± SDs. Two-tailed Student's t test was performed on all of the data represented.
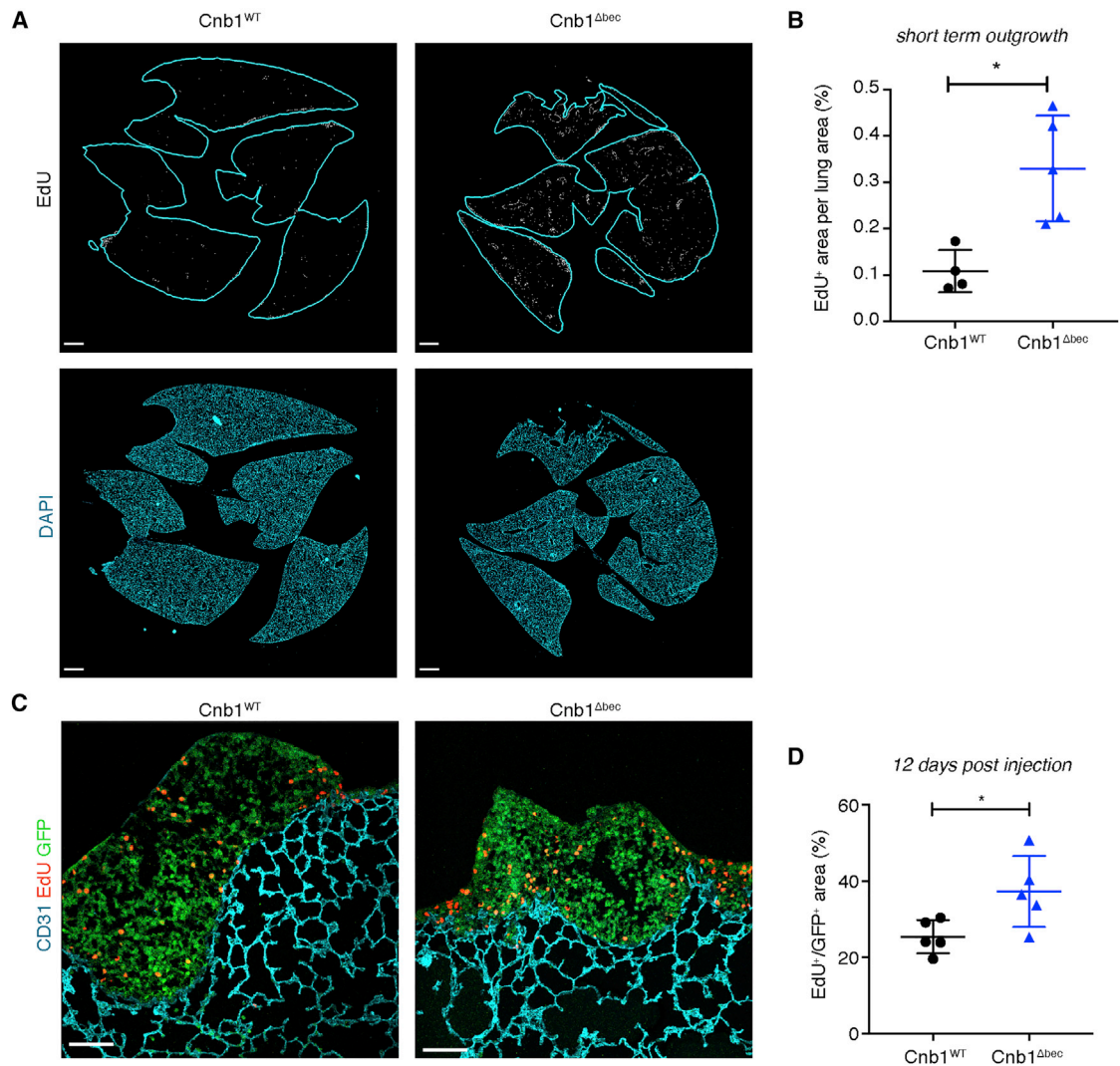
Scale bars: (C and G) 1 mm.

Figure 5. Endothelial Calcineurin Signaling Restricts the Proliferation of Micrometastases in the Lung

(A) Representative images of lung sections from the short-term (day 12) metastasis outgrowth experiment, stained for EdU (white) and for DAPI (blue).

(B) Proliferation is increased in Cnb1$^{\Delta bec}$ lungs injected for 12 days with B16F10 and with tamoxifen injection at day 5. *p = 0.0110; n = 4 Cnb1^{WT}; n = 5 Cnb1$^{\Delta bec}$.

(C) Representative images of B16F10-GFP metastasis in Cnb1^{WT} and Cnb1$^{\Delta bec}$ lungs. Immunofluorescent staining for DNA (blue), EdU (red), and GFP (green).

(D) Quantification of tumor cell proliferation in Cnb1$^{\Delta bec}$ and WT lungs 12 days after tumor cell injection. *p = 0.0329; n = 5 Cnb1^{WT}; n = 5 Cnb1$^{\Delta bec}$. The EdU^{+} area was normalized to the GFP^{+} area.

ns, not significant; error bars represent means ± SDs. Two-tailed Student's t test was performed on all of the data represented.

Scale bars: (A) 1 mm, (C) 100 μm.

mice (Figure 6B). Calcineurin inactivation significantly decreased the endothelial expression of *Bmp2*, while the expression of other previously published target genes such as *TissueF*, *Angpt2*, or *Thbs1* was not modified (Figure 6B).

Bmp2 Inhibits Tumor Cell Growth in 3D

Lung BMP signaling maintains cancer cells in a dormant state by preventing their self-renewal (Gao et al., 2012). Based on this finding and our own observations, we selected BMP2 as a potentially important calcineurin target during tumor progression. BMP2 treatment strongly activated Smad-1/5 phosphorylation in B16F10 cells (Figure 6C), which was inhibited by

dorsomorphin homolog 1 (DMH1), a small molecule antagonist targeting the activation of BMP type I receptors (Hao et al., 2010). However, BMP2 did not affect melanoma cell growth in a 2-dimensional (2D) monolayer (Figure 6D). As metastases grow in a 3D environment, we studied whether BMP2 affects the ability of B16F10-luc cells, tagged with firefly luciferase to form spheroids in Matrigel. In 3D conditions, the addition of BMP2 significantly decreased luciferase signal and spheroid growth (Figures 6E–6G). BMP2 treatment significantly reduced the number of large 3D colonies, whereas the number of small colonies was increased, indicating that BMP signaling inhibits spheroid outgrowth (Figure 6G). The inhibition of spheroid
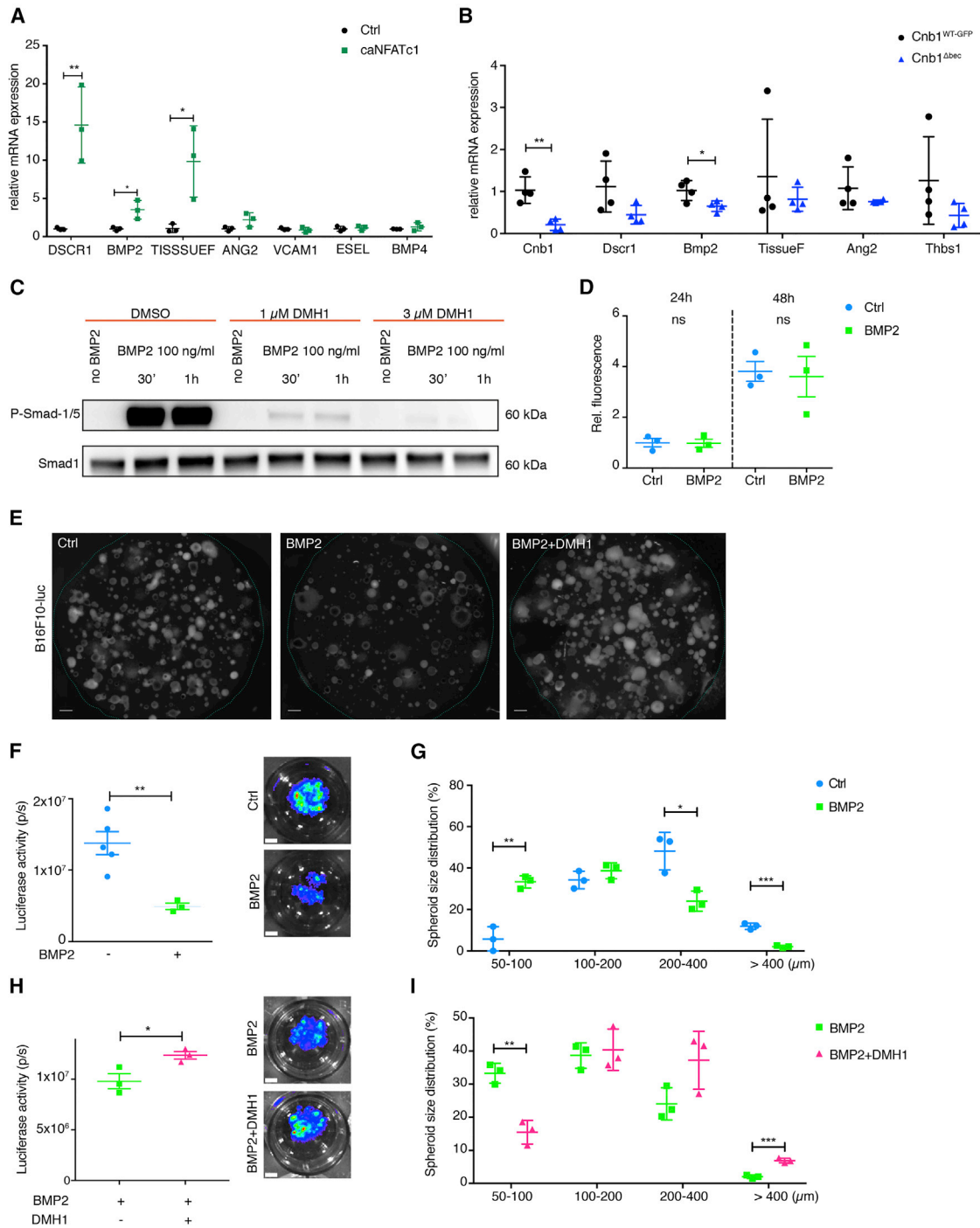
Figure 6. Calcineurin Regulates Bmp2 Expression in the Endothelium, a Potent Inhibitor of Tumor Cell Growth

(A) caNFATc1 induces the expression of *DSRC1*, *BMP2*, and *TISSUEF* in HUVECs. The qRT-PCR analyses of the indicated genes; n = 3, **p = 0.0091 *DSCR1*, *p = 0.0257 *BMP2*, and *p = 0.0318 *TISSUEF*.

(B) Loss of calcineurin reduces the expression of *Cnb1*, *Dscr1*, and *Bmp2* in the BEC-2 population of lung ECs. *p = 0.0316, **p = 0.0029; n = 3 Cnb1^{WT-GFP}; n = 4 Cnb1$^{\Delta bec}$.

(C) BMP2 induces the phosphorylation of Smad-1/5 in B16F10 cells. Cells were treated with 100 ng/mL BMP2 in the presence or absence of 1 or 3 μM DMH1. Western blot for the indicated proteins.

(D) BMP2 does not affect B16F10 cell growth in 2D. Cells were treated with vehicle or 100 ng/mL BMP2 for 24 and 48 h and analyzed by CyQuant DNA-based assay.

(E) BMP2 reduces B16F10 cell growth in 3D. Representative images of B16F10 spheroids treated with 100 ng/mL BMP2, BMP2 + 3 μM DMH1, or vehicle.

(legend continued on next page)

expansion by BMP2 was rescued by the combined treatment with DMH1 (Figures 6E, 6H, and 6I). Similar to B16F10 cells, BMP2 treatment activated Smad-1/5 signaling and reduced the 3D growth of MC38 cells, which was rescued by DMH1 (Figures S7A–S7C).

BMP2 Signaling Promotes Melanoma Cell Differentiation

To further evaluate the pathways affected by BMP2 in melanoma cells, we compared the transcriptomes of control and BMP2-treated B16F10 3D spheroids. The expression of 54 and 72 genes was significantly up- or downregulated in response to BMP2 (false discovery rate [FDR] <0.05, fold change [FC] >2). As expected, BMP2 target genes ID2, SMAD6, and ATOH8 were significantly induced (Figure 7A; Koch et al., 2016). BMP2 strongly repressed the nuclear factor κB (NF-κB) pathway, previously implicated in melanoma cell survival, invasion, and metastasis (Figure 7B; Amiri and Richmond, 2005). In agreement with reduced spheroid growth, BMP2 downregulated the expression of genes involved in mitosis, targets of CMYC and E2F transcription factors, and genes associated with the mTOR complex 1 pathway (Figure 7B). BMP2 treatment also repressed gene signatures associated with hypoxia and glycolysis and oxidative phosphorylation, indicating overall reduced metabolic activity (Figure 7B). We observed significantly increased expression of genes important for melanogenesis, such as Serpin F1, TYR, GPR143, Mlph, SLC45a2, and MITF (Figure 7A; Chen et al., 2016; Fernández-Barral et al., 2014; Kondo and Hearing, 2011). Analysis of Gene Ontology (GO) terms for biological processes revealed that 5 of 9 GO terms related to pigmentation and melanogenesis were significantly induced in BMP2-treated melanoma cells, indicating increased differentiation (Figure 7C; Table S1). Human melanomas can be categorized into 4 progressive subtypes along a differentiation trajectory that resembles different stages of melanocyte embryonic development (Tsoi et al., 2018). The BMP2-dependent transcriptional signature of B16F10 cells correlated best with a highly differentiated human melanocytic subtype, followed by transitory, neural crest-like, and undifferentiated subtypes (Figure 7D). These data validate the pro-differentiation effect of BMP2 in melanoma cells. We evaluated the differentiation of B16F10 metastases *in vivo* by staining for levodopa (L-DOPA) as a readout for tyrosinase activity and melanin biosynthesis (Lanza et al., 2017). We confirmed that upon calcineurin deletion, and thus reduced BMP2 expression, lung metastases had reduced tyrosinase activity (Figures 7E and 7F). Our data indicate that BMP2 signaling inhibits the 3D growth of cancer cells by promoting differentiation along melanocytic lineage and reducing metabolic activity and cell-cycle progression.

Endothelial BMP2 Regulates Retinal Angiogenesis and Metastatic Colonization

To study the role of endothelial-derived BMP2 *in vivo* we generated $Bmp2^{flox/flox}$; $Pdgfb$-iCre^{ERT2} mice (Bmp2$^{\Delta bec}$) and analyzed retinal angiogenesis and metastatic colonization. In postnatal retina, vascular density but not radial expansion was significantly reduced upon endothelial inactivation of BMP2, and there was a tendency toward an increased number of collagen IV$^+$ empty sleeves (Figures 7G–7J). Most important, in lung colonization experiments, we observed that the loss of endothelial BMP2 enhanced the formation of metastases (Figures 7K and 7L). The effect of endothelial Bmp2 loss on metastatic outgrowth was less pronounced compared to calcineurin inactivation (Figures 3D and 3E). These *in vivo* results indicate that BMP2 is an important effector molecule acting downstream of calcineurin in ECs, although additional calcineurin targets are also likely involved.

DISCUSSION

In this work, we used an EC-specific calcineurin deletion model to investigate the role of this signaling pathway in physiological and pathological angiogenesis and tumor metastasis. We report that angiogenic sprouting and primary tumor growth are not significantly affected by the absence of calcineurin in ECs. However, both in physiological and pathological situations, calcineurin modulates vascular regression. Most important, our study shows that the ablation of calcineurin in the endothelium promotes metastatic outgrowth.

Earlier work suggested that calcineurin has an essential role in sprouting angiogenesis *in vitro* and *in vivo* (Hernández et al., 2001; Mena et al., 2014). However, during embryogenesis, calcineurin is crucial for the formation of heart valves and coronary vessels and for the maturation of lymphatic vessels, but it is dispensable for the growth of other vascular beds (Bushdid et al., 2003; de la Pompa et al., 1998; Norrmén et al., 2009; Sabine et al., 2012; Zeini et al., 2009). Here, in a model of physiological retinal angiogenesis, we show that calcineurin is dispensable for EC proliferation and sprouting. In contrast, vessel regression was affected, indicating that endothelial calcineurin signaling is involved in vessel stabilization and remodeling. In addition to the VEGF-A/VEGFR2 pathway, calcineurin acts downstream of the non-canonical Wnt pathway in several cell types, including blood ECs (De, 2011; Scholz et al., 2016), and defective vessel stabilization was observed in models with an EC-specific ablation of non-canonical WNT signaling components (Franco et al., 2016; Korn et al., 2014; Scholz et al., 2016). Loss of endothelial calcineurin also leads to increased pericyte association with empty sleeves, indicating that this pathway

---

(F) Quantification of B16F10-luc spheroid growth. Bioluminescence was quantified by Xenogen imaging. **p = 0.0066; n = 5 Ctrl; n = 3 BMP2.

(G) BMP2 treatment reduces B16F10 spheroid expansion. Quantification of the number of small (50–100 μm), intermediate (100–200 μm), and large colonies (>200 μm). *p = 0.0157; **p = 0.0019; ***p = 0.0002; n = 3 per treatment condition.

(H) DMH1 rescues the decreased B16F10-luc spheroid formation by BMP2. Bioluminescence was quantified by Xenogen imaging. *p = 0.0366; n = 3 BMP2, n = 3 DMH1.

(I) DMH1 treatment reduces the number of B1610 small spheroids and increases the number of larger spheroids (>400 μm) compared to BMP2 treatment. **p = 0.0027, ***p = 0.0006; n = 3 per treatment condition.

Error bars represent means ± SDs. Two-tailed Student's t test was performed on all of the data represented. Scale bars: (E) 200 μm, (F and H) 2 mm.
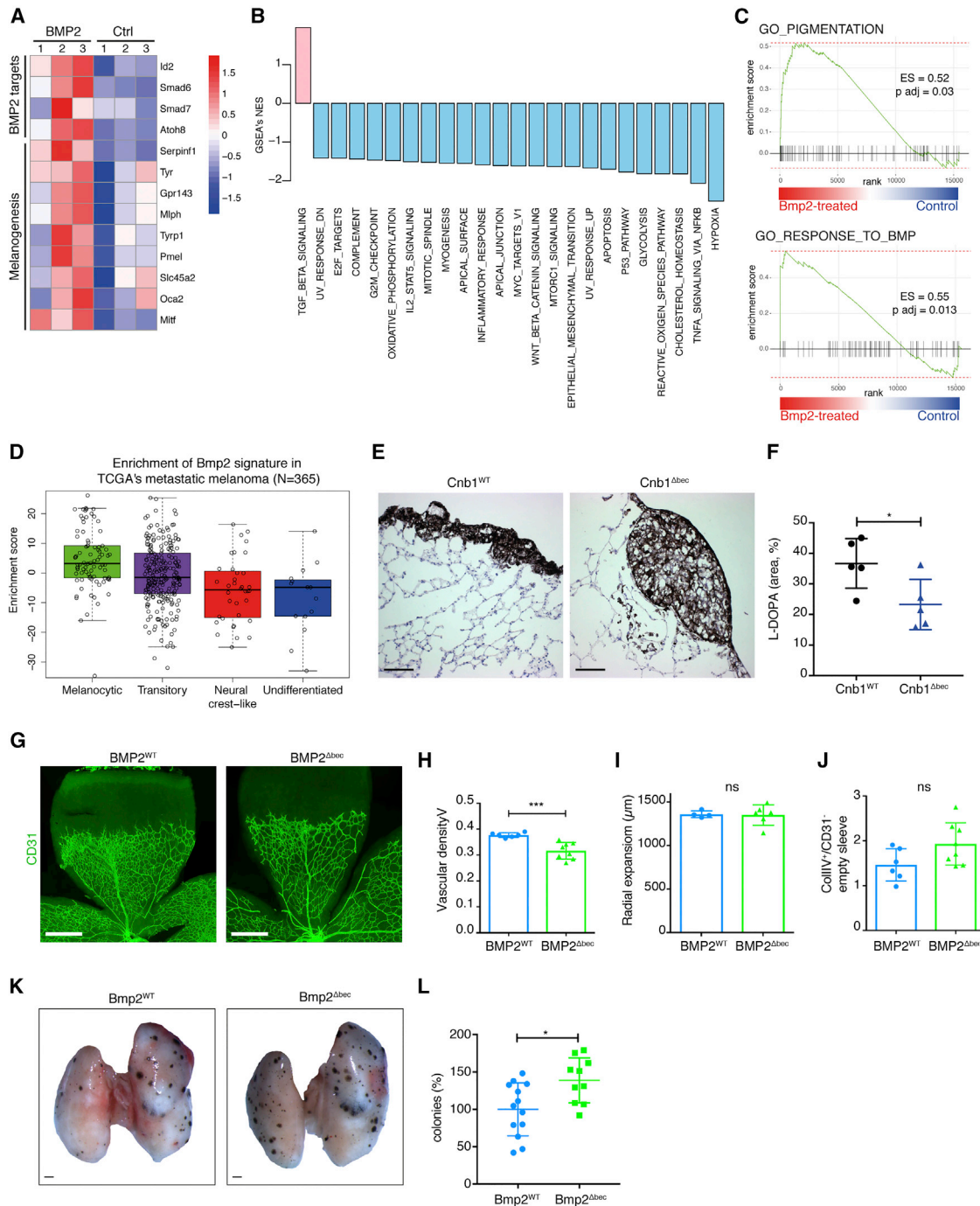
Figure 7. BMP2 Regulates the Growth and Differentiation of Melanoma Cells and Retinal Angiogenesis

(A) Heatmap of BMP2 targets and melanogenesis-related genes induced by BMP2 in B16F10 cells.

(B) Gene set enrichment analysis (GSEA) waterfall plot for the hallmark gene sets significantly affected by BMP2 in B16F10 3D spheroids; upregulated (pink) and downregulated (blue) pathways with adjusted p < 0.05.

(C) GO biological processes "Pigmentation" and "Response to Bmp" are significantly enriched in BMP2-treated B16F10 spheroids.

(D) Signature of BMP2-treated B16F10 spheroids is enriched in human differentiated melanomas.

(E) Representative pictures of L-DOPA staining in Cnb1^{WT} and Cnb1$^{\Delta bec}$ lungs 12 days post-i.v. injection.

(F) Tyrosinase activity is reduced in B16F10 metastases in Cnb1$^{\Delta bec}$ lungs 12 days post-i.v. injection; n = 5 Cnb1^{WT}; n = 5 Cnb1$^{\Delta bec}$.

(G) Representative images of a P5 retina leaflet from BMP2^{WT} or BMP2$^{\Delta bec}$ mice, staining for CD31 (green).

(H) Reduced vascular density in P5 BMP2$^{\Delta bec}$ retina. ***p = 0.0008, n = 6 BMP2^{WT}; n = 8 BMP2$^{\Delta bec}$.

(I) Radial expansion is similar in BMP2^{WT} and BMP2$^{\Delta bec}$ retinas; n = 4 BMP2^{WT}; n = 6 BMP2$^{\Delta bec}$.

(legend continued on next page)

regulates mural cell behavior. It is not yet clear whether pericytes from remodeling vessels remain in the empty sleeves and undergo apoptosis or migrate onto the surviving vessel (Korn and Augustin, 2015). Our findings indicate that pericytes remain in the empty sleeves and that upon calcineurin deletion, these pericytes would have better survival rates.

Pharmacological calcineurin inhibition decreased tumor angiogenesis and tumor growth in several studies (Courtwright et al., 2009; Medyouf et al., 2007). However, in our model, despite the efficient deletion of Cnb1 and the inhibition of calcineurin/NFAT signaling in the tumor endothelium, vascular density was not significantly affected, whereas vascular stabilization was decreased. The tumor phenotype of Cnb1$^{\Delta bec}$ mice is thus also rather similar to that of mice with deficient endothelial non-canonical WNT signaling, in which a defective vessel stabilization and only a minor effect on primary tumor growth have been reported (Scholz et al., 2016). It is conceivable that the pharmacological inhibition of calcineurin blunts tumor growth in cancers, in which calcineurin/NFAT drives malignant cell proliferation, such as in T and B cell lymphomas (Medyouf et al., 2007), or alternatively, when the tumor vasculature is especially sensitive to the loss of non-canonical WNT signaling.

A more intriguing part of our study was that endothelial calcineurin restricts the outgrowth of metastases. This may explain in part the clinical observations that solid organ transplant recipients are both more susceptible to develop *de novo* cancer and have a more aggressive course of the disease in comparison to the general population (Chapman et al., 2013; Sherston et al., 2014). Studies of *Dscr1*$^{-/-}$ mice with hyperactive NFAT signaling proposed that the increased production of endothelial Ang2 drives cancer cell extravasation by increasing lung vascular permeability (Minami et al., 2013). In contrast, in mice with endothelial calcineurin inactivation, we did not observe significant changes in endothelial *Angpt2* expression or metastatic cancer cell behavior up to 12 days after intravenous injection, which argues against the importance of calcineurin during the early stages of metastasis. Rather, we observed an increased outgrowth of metastatic colonies in Cnb1$^{\Delta bec}$ mice during a critical time window, after which metastatic growth becomes independent of endothelium-derived paracrine signals.

Mechanistically, we propose that intact calcineurin signaling in lung ECs induces the expression of BMP2, which restrains the outgrowth of micrometastases by promoting cell differentiation. Calcineurin activation induces BMP2 in ECs *in vitro* and *in vivo*, and BMP2 treatment potently suppresses the 3D growth of cancer cells. Furthermore, the analyses of melanoma cell transcriptomes revealed that together with reducing metabolic activity and cell-cycle progression, BMP2 directed differentiation along the melanocytic lineage. In addition, metastases in Cnb1$^{\Delta bec}$ lungs had lower tyrosinase activity, confirming the reduced differentiation of B16F10 cells when Bmp2 expression downstream of

calcineurin is impaired. Most important, direct *in vivo* inactivation of endothelial Bmp2 increased the metastatic potential of cancer cells, although to a lesser extent than calcineurin deletion. We have not confirmed whether endothelial Bmp2 deletion directly affects the differentiation of B16F10 *in vivo*. However, comparison of the BMP2-dependent transcriptional signature of B16F10 cells with human melanomas (Tsoi et al., 2018) showed that it correlates best with a melanocytic differentiated subtype. Calcineurin activates all 4 NFAT isoforms (Mancini and Toker, 2009), and previous studies suggested the roles both for NFATc1 and NFATc3 in vascular remodeling and angiogenesis (Bushdid et al., 2003; Scholz et al., 2016). The question of which NFAT isoform relays calcineurin activation in the endothelium during metastatic outgrowth thus merits future investigation.

From the clinical point of view, the use of calcineurin inhibitors for immunosuppressive therapy in solid organ transplant recipients is strongly associated with increased *de novo* malignancies, including melanomas, and especially with a more aggressive course of disease (Chapman et al., 2013; Sherston et al., 2014; Tremblay et al., 2002). Given the important roles of calcineurin/NFAT in immune cells, impaired anti-tumor immunity is conceivably the main culprit leading to the development of cancers in transplant recipients. In addition, our data argue that the loss of endothelial calcineurin/NFAT signaling directly contributes to the progression of at least some cancer types because of the loss of paracrine inhibitory communication between endothelial and cancer cells.

In conclusion, we demonstrate the role of calcineurin in the postnatal vasculature using an inducible endothelial-specific deletion model. In both physiological retinal and pathological tumor vasculatures, calcineurin is dispensable for sprouting angiogenesis and is mostly implicated in vessel stabilization, which does not affect primary tumor growth. EC calcineurin activation restrains the outgrowth of metastases, suggesting that post-transplantation immunosuppressive therapy also directly targets the endothelium, which is crucial for initial metastasis formation, and is independent of immune cells.

STAR★METHODS

Detailed methods are provided in the online version of this paper and include the following:

(J) Quantification of empty sleeves in BMP2^{WT} and BMP2$^{\Delta bec}$ retinas. The number of CD31$^-$, collagen IV$^+$ areas was normalized to the total vascularized area; n = 6 BMP2^{WT}; n = 8 BMP2$^{\Delta bec}$.

(K) Representative images of Bmp2^{WT} and Bmp2$^{\Delta bec}$ lungs 12 days after B16F10 injection.

(L) Quantification of lung metastases in Bmp2^{WT} and Bmp2$^{\Delta bec}$ 12 days post-i.v. injection. *p = 0.0113, n = 13 Bmp2^{WT}; n = 10 Bmp2$^{\Delta bec}$. Data combined from 3 independent experiments.

Error bars represent means ± SDs. Two-tailed Student's t test was performed on (F), (H–J), and (L). Scale bars: (E) 100 μm, (G) 500 μm, (K) 1 mm.

SUPPLEMENTAL INFORMATION

ACKNOWLEDGMENTS

AUTHOR CONTRIBUTIONS

S.H., S.C., and T.V.P. designed the study. S.H. performed the experiments, analyzed and interpreted the data, and wrote the manuscript. S.C., B.P.-L., and L.W. performed the experiments and analyzed and interpreted the data. A.S., C.F., and H.G. performed the experiments and analyzed the data. N.Z., S.N., and M.D. performed the bioinformatics analysis. T.V.P. directed the study, interpreted the data, and wrote the manuscript. All of the authors revised the manuscript critically.

DECLARATION OF INTERESTS

REFERENCES

Amiri, K.I., and Richmond, A. (2005). Role of nuclear factor-κ B in melanoma. Cancer Metastasis Rev. 24, 301–313.

Armulik, A., Genové, G., and Betsholtz, C. (2011). Pericytes: developmental, physiological, and pathological perspectives, problems, and promises. Dev. Cell 21, 193–215.

Baek, K.-H., Zaslavsky, A., Lynch, R.C., Britt, C., Okada, Y., Siarey, R.J., Lensch, M.W., Park, I.-H., Yoon, S.S., Minami, T., et al. (2009). Down's syndrome suppression of tumour growth and the role of the calcineurin inhibitor DSCR1. Nature 459, 1126–1130.

Baluk, P., Morikawa, S., Haskell, A., Mancuso, M., and McDonald, D.M. (2003). Abnormalities of basement membrane on blood vessels and endothelial sprouts in tumors. Am. J. Pathol. 163, 1801–1815.

Bernier-Latmani, J., Cisarovsky, C., Demir, C.S., Bruand, M., Jaquet, M., Davanture, S., Ragusa, S., Siegert, S., Dormond, O., Benedito, R., et al. (2015). DLL4 promotes continuous adult intestinal lacteal regeneration and dietary fat transport. J. Clin. Invest. 125, 4572–4586.

Bray, N.L., Pimentel, H., Melsted, P., and Pachter, L. (2016). Near-optimal probabilistic RNA-seq quantification. Nat. Biotechnol. 34, 525–527.

Bushdid, P.B., Osinska, H., Waclaw, R.R., Molkentin, J.D., and Yutzey, K.E. (2003). NFATc3 and NFATc4 are required for cardiac development and mitochondrial function. Circ. Res. 92, 1305–1313.

Cerami, E., Gao, J., Dogrusoz, U., Gross, B.E., Sumer, S.O., Aksoy, B.A., Jacobsen, A., Byrne, C.J., Heuer, M.L., Larsson, E., et al. (2012). The cBio cancer genomics portal: an open platform for exploring multidimensional cancer genomics data. Cancer Discov. 2, 401–404.

Chapman, J.R., Webster, A.C., and Wong, G. (2013). Cancer in the transplant recipient. Cold Spring Harb. Perspect. Med. 3, a015677.

Chen, T., Wang, H., Liu, Y., Zhao, B., Zhao, Y., Fan, R., Wang, P., and Dong, C. (2016). Ocular Albinism Type 1 Regulates Melanogenesis in Mouse Melanocytes. Int. J. Mol. Sci. 17, E1596.

Claxton, S., Kostourou, V., Jadeja, S., Chambon, P., Hodivala-Dilke, K., and Fruttiger, M. (2008). Efficient, inducible Cre-recombinase activation in vascular endothelium. Genesis 46, 74–80.

Courtwright, A., Siamakpour-Reihani, S., Arbiser, J.L., Banet, N., Hilliard, E., Fried, L., Livasy, C., Ketelsen, D., Nepal, D.B., Perou, C.M., et al. (2009). Secreted frizzle-related protein 2 stimulates angiogenesis via a calcineurin/NFAT signaling pathway. Cancer Res. 69, 4621–4628.

De, A. (2011). Wnt/Ca2+ signaling pathway: a brief overview. Acta Biochim. Biophys. Sin. (Shanghai) 43, 745–756.

de la Pompa, J.L., Timmerman, L.A., Takimoto, H., Yoshida, H., Elia, A.J., Samper, E., Potter, J., Wakeham, A., Marengere, L., Langille, B.L., et al. (1998). Role of the NF-ATc transcription factor in morphogenesis of cardiac valves and septum. Nature 392, 182–186.

De Palma, M., Biziato, D., and Petrova, T.V. (2017). Microenvironmental regulation of tumour angiogenesis. Nat. Rev. Cancer 17, 457–474.

Durinck, S., Moreau, Y., Kasprzyk, A., Davis, S., De Moor, B., Brazma, A., and Huber, W. (2005). BioMart and Bioconductor: a powerful link between biological databases and microarray data analysis. Bioinformatics 21, 3439–3440.

Durinck, S., Spellman, P.T., Birney, E., and Huber, W. (2009). Mapping identifiers for the integration of genomic datasets with the R/Bioconductor package biomaRt. Nat. Protoc. 4, 1184–1191.

Fernández-Barral, A., Orgaz, J.L., Baquero, P., Ali, Z., Moreno, A., Tiana, M., Gómez, V., Riveiro-Falkenbach, E., Cañadas, C., Zazo, S., et al. (2014). Regulatory and functional connection of microphthalmia-associated transcription factor and anti-metastatic pigment epithelium derived factor in melanoma. Neoplasia 16, 529–542.

Franco, C.A., Jones, M.L., Bernabeu, M.O., Geudens, I., Mathivet, T., Rosa, A., Lopes, F.M., Lima, A.P., Ragab, A., Collins, R.T., et al. (2015). Dynamic endothelial cell rearrangements drive developmental vessel regression. PLoS Biol. 13, e1002125.

Franco, C.A., Jones, M.L., Bernabeu, M.O., Vion, A.-C., Barbacena, P., Fan, J., Mathivet, T., Fonseca, C.G., Ragab, A., Yamaguchi, T.P., et al. (2016). Noncanonical Wnt signalling modulates the endothelial shear stress flow sensor in vascular remodelling. eLife 5, e07727.

Fruttiger, M. (2007). Development of the retinal vasculature. Angiogenesis 10, 77–88.

Gao, H., Chakraborty, G., Lee-Lim, A.P., Mo, Q., Decker, M., Vonica, A., Shen, R., Brogi, E., Brivanlou, A.H., and Giancotti, F.G. (2012). The BMP inhibitor Coco reactivates breast cancer cells at lung metastatic sites. Cell 150, 764–779.

Gao, J., Aksoy, B.A., Dogrusoz, U., Dresdner, G., Gross, B., Sumer, S.O., Sun, Y., Jacobsen, A., Sinha, R., Larsson, E., et al. (2013). Integrative analysis of complex cancer genomics and clinical profiles using the cBioPortal. Sci. Signal. 6, pl1.

Gerhardt, H., Golding, M., Fruttiger, M., Ruhrberg, C., Lundkvist, A., Abramsson, A., Jeltsch, M., Mitchell, C., Alitalo, K., Shima, D., and Betsholtz, C. (2003). VEGF guides angiogenic sprouting utilizing endothelial tip cell filopodia. J. Cell Biol. 161, 1163–1177.

Graupera, M., Guillermet-Guibert, J., Foukas, L.C., Phng, L.-K., Cain, R.J., Salpekar, A., Pearce, W., Meek, S., Millan, J., Cutillas, P.R., et al. (2008). Angiogenesis selectively requires the p110alpha isoform of PI3K to control endothelial cell migration. Nature 453, 662–666.

Gray, E.E., Friend, S., Suzuki, K., Phan, T.G., and Cyster, J.G. (2012). Subcapsular sinus macrophage fragmentation and CD169+ bleb acquisition by closely associated IL-17-committed innate-like lymphocytes. PLoS One 7, e38258.

Hao, J., Ho, J.N., Lewis, J.A., Karim, K.A., Daniels, R.N., Gentry, P.R., Hopkins, C.R., Lindsley, C.W., and Hong, C.C. (2010). In vivo structure-activity relationship study of dorsomorphin analogues identifies selective VEGF and BMP inhibitors. ACS Chem. Biol. 5, 245–253.

Hernández, G.L., Volpert, O.V., Iñiguez, M.A., Lorenzo, E., Martínez-Martínez, S., Grau, R., Fresno, M., and Redondo, J.M. (2001). Selective inhibition of vascular endothelial growth factor-mediated angiogenesis by cyclosporin A: roles of the nuclear factor of activated T cells and cyclooxygenase 2. J. Exp. Med. 193, 607–620.

Jurisic, G., Maby-El Hajjami, H., Karaman, S., Ochsenbein, A.M., Alitalo, A., Siddiqui, S.S., Ochoa Pereira, C., Petrova, T.V., and Detmar, M. (2012). An unexpected role of semaphorin3a-neuropilin-1 signaling in lymphatic vessel maturation and valve formation. Circ. Res. 111, 426–436.

Kerr, B.A., West, X.Z., Kim, Y.-W., Zhao, Y., Tischenko, M., Cull, R.M., Phares, T.W., Peng, X.-D., Bernier-Latmani, J., Petrova, T.V., et al. (2016). Stability and function of adult vasculature is sustained by Akt/Jagged1 signalling axis in endothelium. Nat. Commun. 7, 10960.

Kitamura, T., Qian, B.-Z., and Pollard, J.W. (2015). Immune cell promotion of metastasis. Nat. Rev. Immunol. 15, 73–86.

Koch, P.-S., Olsavszky, V., Ulbrich, F., Sticht, C., Demory, A., Leibing, T., Henzler, T., Meyer, M., Zierow, J., Schneider, S., et al. (2016). Angiocrine Bmp2 signaling in murine liver controls normal iron homeostasis. Blood 129, 415–419.

Kondo, T., and Hearing, V.J. (2011). Update on the regulation of mammalian melanocyte function and skin pigmentation. Expert. Rev. Dermatol. 6, 97–108.

Korn, C., and Augustin, H.G. (2015). Mechanisms of Vessel Pruning and Regression. Dev. Cell 34, 5–17.

Korn, C., Scholz, B., Hu, J., Srivastava, K., Wojtarowicz, J., Arnsperger, T., Adams, R.H., Boutros, M., Augustin, H.G., and Augustin, I. (2014). Endothelial cell-derived non-canonical Wnt ligands control vascular pruning in angiogenesis. Development 141, 1757–1766.

Lanza, B., Ragnelli, A.M., Priore, M., and Aimola, P. (2017). Morphological and histochemical investigation of the response of Olea europaea leaves to fungal attack by Spilocaea oleagina. Plant Pathol. 66, 1239–1247.

Liberzon, A., Birger, C., Thorvaldsdóttir, H., Ghandi, M., Mesirov, J.P., and Tamayo, P. (2015). The Molecular Signatures Database (MSigDB) hallmark gene set collection. Cell Syst. 1, 417–425.

Love, M.I., Huber, W., and Anders, S. (2014). Moderated estimation of fold change and dispersion for RNA-seq data with DESeq2. Genome Biol. 15, 550.

Ma, L., and Martin, J.F. (2005). Generation of a Bmp2 conditional null allele. Genesis 42, 203–206.

Mancini, M., and Toker, A. (2009). NFAT proteins: emerging roles in cancer progression. Nat. Rev. Cancer 9, 810–820.

Medyouf, H., Alcalde, H., Berthier, C., Guillemin, M.C., dos Santos, N.R., Janin, A., Decaudin, D., de Thé, H., and Ghysdael, J. (2007). Targeting calcineurin activation as a therapeutic strategy for T-cell acute lymphoblastic leukemia. Nat. Med. 13, 736–741.

Mena, M.-P., Papiewska-Pajak, I., Przygodzka, P., Kozaczuk, A., Boncela, J., and Cierniewski, C.S. (2014). NFAT2 regulates COX-2 expression and modulates the integrin repertoire in endothelial cells at the crossroads of angiogenesis and inflammation. Exp. Cell Res. 324, 124–136.

Minami, T., Horiuchi, K., Miura, M., Abid, M.R., Takabe, W., Noguchi, N., Kohro, T., Ge, X., Aburatani, H., Hamakubo, T., et al. (2004). Vascular endothelial growth factor- and thrombin-induced termination factor, Down syndrome critical region-1, attenuates endothelial cell proliferation and angiogenesis. J. Biol. Chem. 279, 50537–50554.

Minami, T., Jiang, S., Schadler, K., Suehiro, J., Osawa, T., Oike, Y., Miura, M., Naito, M., Kodama, T., and Ryeom, S. (2013). The calcineurin-NFAT-angiopoietin-2 signaling axis in lung endothelium is critical for the establishment of lung metastases. Cell Rep. 4, 709–723.

Monticelli, S., and Rao, A. (2002). NFAT1 and NFAT2 are positive regulators of IL-4 gene transcription. Eur. J. Immunol. 32, 2971–2978.

Norrmén, C., Ivanov, K.I., Cheng, J., Zangger, N., Delorenzi, M., Jaquet, M., Miura, N., Puolakkainen, P., Horsley, V., Hu, J., et al. (2009). FOXC2 controls formation and maturation of lymphatic collecting vessels through cooperation with NFATc1. J. Cell Biol. 185, 439–457.

Ryeom, S., Baek, K.-H., Rioth, M.J., Lynch, R.C., Zaslavsky, A., Birsner, A., Yoon, S.S., and McKeon, F. (2008). Targeted deletion of the calcineurin inhibitor DSCR1 suppresses tumor growth. Cancer Cell 13, 420–431.

Sabine, A., Agalarov, Y., Maby-El Hajjami, H., Jaquet, M., Hägerling, R., Pollmann, C., Bebber, D., Pfenniger, A., Miura, N., Dormond, O., et al. (2012). Mechanotransduction, PROX1, and FOXC2 cooperate to control connexin37 and calcineurin during lymphatic-valve formation. Dev. Cell 22, 430–445.

Scholz, B., Korn, C., Wojtarowicz, J., Mogler, C., Augustin, I., Boutros, M., Niehrs, C., and Augustin, H.G. (2016). Endothelial RSPO3 Controls Vascular Stability and Pruning through Non-canonical WNT/Ca(2+)/NFAT Signaling. Dev. Cell 36, 79–93.

Schweighofer, B., Testori, J., Sturtzel, C., Sattler, S., Mayer, H., Wagner, O., Bilban, M., and Hofer, E. (2009). The VEGF-induced transcriptional response comprises gene clusters at the crossroad of angiogenesis and inflammation. Thromb. Haemost. 102, 544–554.

Sergushichev, A. (2016). An algorithm for fast preranked gene set enrichment analysis using cumulative statistic calculation. bioRxiv. https://doi.org/10.1101/060012.

Sherston, S.N., Carroll, R.P., Harden, P.N., and Wood, K.J. (2014). Predictors of cancer risk in the long-term solid-organ transplant recipient. Transplantation 97, 605–611.

Soneson, C., Love, M.I., and Robinson, M.D. (2015). Differential analyses for RNA-seq: transcript-level estimates improve gene-level inferences. F1000Res. 4, 1521.

Subramanian, A., Tamayo, P., Mootha, V.K., Mukherjee, S., Ebert, B.L., Gillette, M.A., Paulovich, A., Pomeroy, S.L., Golub, T.R., Lander, E.S., and Mesirov, J.P. (2005). Gene set enrichment analysis: a knowledge-based approach for interpreting genome-wide expression profiles. Proc. Natl. Acad. Sci. USA 102, 15545–15550.

Suehiro, J., Kanki, Y., Makihara, C., Schadler, K., Miura, M., Manabe, Y., Aburatani, H., Kodama, T., and Minami, T. (2014). Genome-wide approaches reveal functional vascular endothelial growth factor (VEGF)-inducible nuclear factor of activated T cells (NFAT) c1 binding to angiogenesis-related genes in the endothelium. J. Biol. Chem. 289, 29044–29059.

Tremblay, F., Fernandes, M., Habbab, F., deB Edwardes, M.D., Loertscher, R., and Meterissian, S. (2002). Malignancy after renal transplantation:

incidence and role of type of immunosuppression. Ann. Surg. Oncol. *9*, 785–788.

Tsoi, J., Robert, L., Paraiso, K., Galvan, C., Sheu, K.M., Lay, J., Wong, D.J.L., Atefi, M., Shirazi, R., Wang, X., et al. (2018). Multi-stage Differentiation Defines Melanoma Subtypes with Differential Vulnerability to Drug-Induced Iron-Dependent Oxidative Stress. Cancer Cell *33*, 890–904.e5.

Vigl, B., Aebischer, D., Nitschké, M., Iolyeva, M., Röthlin, T., Antsiferova, O., and Halin, C. (2011). Tissue inflammation modulates gene expression of lymphatic endothelial cells and dendritic cell migration in a stimulus-dependent manner. Blood *118*, 205–215.

Zaichuk, T.A., Shroff, E.H., Emmanuel, R., Filleur, S., Nelius, T., and Volpert, O.V. (2004). Nuclear factor of activated T cells balances angiogenesis activation and inhibition. J. Exp. Med. *199*, 1513–1522.

Zeini, M., Hang, C.T., Lehrer-Graiwer, J., Dao, T., Zhou, B., and Chang, C.-P. (2009). Spatial and temporal regulation of coronary vessel formation by calcineurin-NFAT signaling. Development *136*, 3335–3345.

Zeng, H., Chattarji, S., Barbarosie, M., Rondi-Reig, L., Philpot, B.D., Miyakawa, T., Bear, M.F., and Tonegawa, S. (2001). Forebrain-specific calcineurin knockout selectively impairs bidirectional synaptic plasticity and working/episodic-like memory. Cell *107*, 617–629.

STAR★METHODS

KEY RESOURCES TABLE

REAGENT or RESOURCE	SOURCE	IDENTIFIER
Antibodies		
Rabbit anti-GAPDH	Sigma	RRID:AB_796208
Rabbit anti-P-Smad-1/5	Cell Signaling	RRID:AB_491015
Rabbit anti-Smad1	Cell Signaling	RRID:AB_10858882
Mouse anti-NFATc1	BD Bioscience	RRID:AB_396478
Rat anti-CD45-PeCy7	eBioscience	RRID:AB_2716950
Rat anti-CD31-Pe	eBioscience	RRID:AB_465631
Gp38-AlexaFluor647	In house	Clone 8.1.1
Rat anti.EpCAM-eFluor450	Biolegend	RRID:AB_10717090
Rat anti-CD31/PECAM-1	BD Bioscience	RRID:AB_396660
Rabbit anti-collagen IV	Millipore	RRID:AB_2276457
Goat anti-CD13/Anpep	R&D systems	RRID:AB_2227288
Rat anti-Icam2	BD Bioscience	RRID:AB_394784
Rabbit anti-cleaved caspase-3	Cell Signaling	RRID:AB_2341188
Rabbit anti-Erg1/2/3	Santa Cruz	RRID:AB_675518
Goat anti-Vegfr2	R&D systems	RRID:AB_355500
Rat anti-GFP	Biolegend	RRID:AB_1279414
Rabbit anti-NG2	Millipore	RRID:AB_91789
Rat anti-CD144	BD Bioscience	RRID:AB_395707
Rat anti-CD45-FITC	BD Bioscience	RRID:AB_394610
Rat anti-CD3ϵ-e660	Biolegend	RRID:AB_492861
Rat anti-CD8α-PerCP-Cy5.5	Biolegend	RRID:AB_2075239
Rat anti-CD4-Alexa Fluor 700	Biolegend	RRID:AB_493701
Rat anti-CD44-Pe-Cy7	Biolegend	RRID:AB_830787
Rat anti-CD62L-Pe	Biolegend	RRID:AB_2270062
Rat anti-B220-Texas Red	Thermo Fisher	RRID:AB_10372805
Rat anti-CD11b-eFluor780	Thermo Fisher	RRID:AB_1603193
Rat anti-Gr1-Alexa647	Biolegend	RRID:AB_389331
Rat anti-Ly6C-PerCP-Cy5.5	Biolegend	RRID:AB_1659241
Rat anti-NK1.1-PEe	Biolegend	RRID:AB_313395
Chemicals, Peptides, and Recombinant Proteins		
DMH1	Tocris	Cat#4126
Recombinant human/mouse/rat-BMP2	R&D	Cat#355-BM
Tamoxifen	Sigma	Cat#T5648
EdU	Santa Cruz	Cat#sc-284628
Matrigel	Corning	Cat#356231
Luciferin	Biosynth	Cat#L-8220
Collagenase A	Roche	Cat#10103586001
Collagenase type IV	Worthington	Cat#LS004188
DNaseI	Sigma	Cat#11284932001
Fluoromount-G	eBioscience	Cat#00-4959-52
L-3,4-dihydroxyphenylalanine	Sigma	Cat#59-92-7
7AAD	eBioscience	Cat#00-6993-50
FITC-IB4	Invitrogen	Cat#I-32450

(Continued on next page)

Continued

REAGENT or RESOURCE	SOURCE	IDENTIFIER
EGM-2 Endothelial Cell Growth Medium-2 BulletKit	Lonza	Cat#3162
CellTracker Orange CMTMR Dye	Invitrogen	Cat#C2927
Critical Commercial Assays		
CyQUANT NF Cell Proliferation Assay Kit	Invitrogen	Cat#C35006
RNA isolation RNeasy plus mini/micro kit	QIAGEN	Cat#74134/ Cat#74034
Transcriptor First strand cDNA synthesis kit	Roche	Cat#04896866001
SYBRGreen PCR Master mix	Kapa Biosystems/ Bioline	Cat#kk4605/ Cat#BIO-92005
Ovation RNA-seq system V2	Nugen	Cat#7102
Illumina TruSeq Stranded mRNA reagents	Illumina	Cat#20020594
Illumina TruSeq SR Cluster Kit v4	Illumina	Cat#GD-401-4001
Deposited Data		
RNaseq B16F10 spheroids Vehicle versus Bmp2 treated	This paper	GEO: GSE117074
Experimental Models: Cell Lines		
HUVECs, polled donor	Lonza	Cat#C2519A
B16F10-luciferase	Perkin Elmer	CVCL_5J39
B16F10-GFP	This paper	N/A
MC38	Lab of Jeffrey Schlom	N/A
MC38-GFP	Lab or Lubor Borsig	N/A
HEK293T	ATCC	Cat#CRL-3216
Experimental Models: Organisms/Strains		
Mouse: Cnb1$^{flox/flox}$ (C57BL/6-Ppp3r1tm1Stl/J)	The Jackson Laboratory	JAX: 006581
Mouse: Tg(Pdgfb-icre/ERT2)1Frut	Lab of Marcus Fruttiger	RRID:MGI:5284856
Mouse: B6;129S4-Bmp2 < tm1Jfm > /J	Lab of Peter Scheiffle	JAX: 016230
Oligonucleotides		
Please see Table S2	This paper	N/A
Software and Algorithms		
Fiji	NIH	RRID:SCR_002285
Prism version 7	Graphpad	RRID:SCR_002798
Living Image Software	PerkinElmer	RRID:SCR_014247
Imaris	Bitplane	RRID:SCR_007370
bcl2fastq Conversion Software	Illumina	RRID:SCR_015058
Other		
caNFATc1 plasmid	Addgene	#11102

CONTACT FOR REAGENT AND RESOURCE SHARING

Further information and requests for resources and reagents should be directed to and will be fulfilled by the Lead Contact, Tatiana V. Petrova (Tatiana.petrova@unil.ch).

EXPERIMENTAL MODEL AND SUBJECT DETAILS

Animal models

Experiments were approved by the Animal Ethics Committee of the Canton of Vaud. Ppp3r1$^{fl/fl}$, BMP2$^{fl/fl}$ and *Pdgfb*-iCre^{ERT2} mice (Claxton et al., 2008; Ma and Martin, 2005; Zeng et al., 2001) were on C57Bl6J background. Adult (5 – 10 weeks old) female mice were injected i.p. with 50 μg/g mouse of tamoxifen in sunflower seed oil (Sigma). Unless indicated otherwise, tamoxifen was administered on day −2 and 0 of cancer cell injection and twice weekly thereafter. Deletion efficiency was confirmed by qRT-PCR of sorted lung and tumor ECs. Pups were injected at P1 and P3 with 20 μl of 2 mg/ml tamoxifen.

Cell culture

Cells were cultured in a sterile incubator at 37°C and 5%CO$_2$. HUVECs (pooled donor, Lonza) were cultured in endothelial growth medium with full supplements (EBM-2, Lonza) and were used up to passage 6. MC38, B16F10-luc and 293T were cultured in DMEM complete (10% FBS, 1% P/S), for B16F10-luc cells zeocin 0.2 mg/ml was added to the culture medium.

METHOD DETAILS

Tumor models

For subcutaneous tumor experiments 5x10^5 B16F10-luc cells (B16F10-luc-G5, Perkin Elmer) in 100 μl PBS were injected in the right flank of the mice. When tumors reached 1 cm^3 mice were sacrificed and perfused intracardially with PBS and 2% PFA. 1 hour prior to sacrifice mice were injected i.p. with 5 μg/g EdU (Life Technologies). Tumors were fixed in 4% PFA for 4h at 4°C, incubated for 12 hours in 30% sucrose and embedded in OCT. For the lung colonization experiments 5x10^5 B16F10-luciferase cells in 200 μl PBS were injected into tail vein, mice were sacrificed after 1, 5, 12 and 19 days and perfused intracardially with PBS and 2% PFA. Lungs were fixed in 4% PFA for 4 hours, left in 30% sucrose for 12 hours, OCT inflated via the trachea and embedded in OCT. In outgrowth experiments the first dose of tamoxifen was administered 5 or 9 days after cancer cell injection, and every two days thereafter. For the 24h tumor cell extravasation assay B16F10-luc were labeled with 15 μm CMTMR (Thermo Fisher) by incubating for 1h at 37°C in serum free medium.

Protein extraction and immunoblotting

Cells were lysed in RIPA buffer (50 mM Tris pH 8, 150 mM NaCl, 1% Triton X-100, 0.5% sodium deoxycholate, and 0.1% sodium dodecyl sulfate) supplemented with phosphatase (PhosSTOP, Roche) and protease (Complete, Roche) inhibitors. Lysates were cleared by centrifugation and supernatants were loaded on 10% SDS-PAGE gels, transferred on nitrocellulose membranes and blocked for 1h at RT in 5% BSA. Membranes were incubated overnight at 4°C with primary antibodies and for 1h at RT with secondary antibodies conjugated to horseradish peroxidase (Dako). Blots were developed using Super Signal West Femto (Thermo Scientific) with a CCD camera (Fusion, Vilber). Details of the antibodies used are provided in the Key Resources Table.

Plasmids and transfections

caNFATc1 construct Addgene plasmid #11102 was subcloned into the pSD44 lentiviral backbone. pSD44-GFP was used as control. Lentiviral particles were prepared by transfecting HEK293T cells with the pSD44 vector of interest and packaging plasmids pSD11 and pSD16. 48h after transfection supernatants were collected and concentrated. For infection 3.5x10^5 HUVECs were plated in a 10cm dish and infected the day after in the presence of polybrene (8 μg/ml) with either GFP or caNFATc1 lentiviruses. The medium was changed 24h later and another 24h later cells were selected with 0.5 μg/ml puromycine for 48 hours.

For the generation of the B16F10-GFP cell line B16F10 were seeded in a 6 well plate and infected the day after with GFP lentivirus. 48h after transfection selection was started with 0.6 μg/ml puromycine, which remained in the culture medium. Single clones were selected to choose cells with the brightest GFP signal.

2D Proliferation analysis

For analysis of cell growth, cells were seeded in 96 well plates at a density of 1000 cells/well, 100 ng/ml rBMP2 (R&D) or vehicle treatment was added for 24 or 48 hours. Live cell number was determined using CyQuant NF DNA-based assay (Invitrogen).

Spheroid formation

500 B16F10 or 300 MC38 cells were plated in 50 μl of 7 mg/ml Matrigel (Corning) and cultured for approximately 10 days, depending on the experiment. 100 ng/ml of mouse rBMP2 (R&D) was added in the presence or absence of 3 μM DMH1 (Tocris) in DMEM complete medium and was changed every other day. At the end of the experiment, the whole well was imaged with a Leica M205FA stereomicroscope, using Leica camera DFC300FXR2 and LAS AF6000 software. For quantification, 3 images per well were taken with a Leica DMI3000 microscope, using a DFC3000G camera and LAS X software. B16F10-luc spheroids were imaged with the Xenogen IVIS Lumina II system after supplementation with 0.3 mg/ml luciferin (Biosynth) and analysis was performed with Living Image software (Perkin Elmer).

Retina preparation

Pups were injected at P1 and P3 with 20 μl of 2 mg/ml tamoxifen in sunflower seed oil. Pups were sacrificed at day 5 and eyeballs were fixed in 4% PFA for 4 hours at 4°C. Retinas were dissected and blocked with blocking buffer (0.5% BSA, 5% donkey serum, 0.3% Triton X-100, 0.1% NaN$_3$) for 6h at 4°C. Primary antibodies were diluted in blocking buffer and incubated overnight at 4°C. Subsequently, retinas were incubated with fluorophore-conjugated Alexa secondary antibodies (Thermo Fisher) in blocking buffer overnight at 4°C and mounted with mounting medium (Fluoromount-G, Invitrogen). Details of the antibodies used are provided in the Key Resources Table.

Cell staining

Cells were grown on glass coverslips, washed once with cold PBS (with calcium chloride and magnesium chloride), fixed for 10 minutes in 4% PFA in PBS, permeabilized for 10 minutes with 0.1% Triton X-100 in PBS, blocked for 30 minutes with blocking buffer (0.5% BSA, 5% donkey serum, 0.3% Triton X-100, 0.1% NaN$_3$) and incubated with primary antibodies for 1h at RT. Cells were then washed 3 × 10 minutes with 0.1% Triton-x PBS and incubated with fluorophore-conjugated Alexa secondary antibodies (Thermo Fisher) in blocking buffer for 1h at RT, washed again for 3 × 10 minutes with 0.1% Triton-x PBS and once with PBS before mounting with mounting medium (Fluoromount-G, Invitrogen). Details of the antibodies used are provided in the Key Resources Table

Immunofluorescent and histochemical staining

8 μm OCT sections were thawed for 20 minutes at RT, fixed for 10 minutes in 4% PFA and washed with 0.3% Triton-x PBS. After blocking for 30 minutes with blocking buffer (0.5% BSA, 5% donkey serum, 0.3% Triton X-100, 0.1% NaN$_3$) slides were incubated with primary antibodies overnight at 4°C in blocking buffer. On day 2, slides were washed 3 x with 0.3% Triton-x PBS for 10 minutes and fluorophore-conjugated Alexa secondary antibodies (Thermo Fisher) were added in blocking buffer for 1h at RT. Slides were washed 3 × 10 minutes with 0.3% Triton-x PBS and once with PBS before mounting.

For the analysis of tyrosinase activity lung cryostat sections were incubated with 5 mM of L-3,4-dihydroxyphenylalanine (L-DOPA, Sigma-Aldrich) in 0.1 mM sodium phosphate buffer at pH 7.4 for 2 h at 37°C; controls were incubated with the buffer alone. The sections were fixed in 4% PFA for 15 min at RT, counterstained with Mayer's hematoxilin and mounted.

qRT-PCR

RNA was isolated using the QIAGEN RNeasy Plus Mini Kit. Reverse transcription was performed using Transcriptor First Strand cDNA Synthesis Kit (Roche). Alternatively, RNA from FACS samples was isolated using the QIAGEN RNeasy Plus Micro Kit and mRNA was amplified using the Ovation RNA-seq system V2 (Nugen). StepOnePlus (Applied Biosystems) and SYBR Green PCR Master Mix (Kapa Biosystems/Bioline) were used for qRT-PCR analyses. Data was normalized to GAPDH (HUVECs) or B2m (FACS samples) using the comparative Ct (ΔΔCt) method. Sequences of PCR primers are provided in Table S2.

RNA-sequencing

RNA quality was assessed on a Fragment Analyzer (Advanced Analytical Technologies, Inc., Ankeny, IA, USA) and all RNAs had a RQN between 9.4 and 10.

RNA-seq libraries were prepared using 500 ng of total RNA and the Illumina TruSeq Stranded mRNA reagents (Illumina; San Diego, California, USA). Cluster generation was performed with the resulting libraries using the Illumina TruSeq SR Cluster Kit v4 reagents and sequenced on the Illumina HiSeq 2500. Sequencing data were demultiplexed using the bcl2fastq Conversion Software (v. 2.20, Illumina; San Diego, California, USA).

Endothelial cell sorting

For sorting of endothelial cells we used the Pdgfb-iCreERT2$^{tg/+}$ (Cnb1^{WT-GFP}) as controls, which express EGFP in the Pdgfb-iCreERT2 construct (Claxton et al., 2008)

For isolation of tumor endothelial cells Cnb1$^{\Delta bec}$ and Cnb1^{WT-GFP} mice were injected s.c. with 5x10^5 B16F10-luc cells and tamoxifen was administered. 7 days after cancer cell injection mice were sacrificed. Following 30 min incubation with 10% collagenase type IV (Worthington) and 50 μg/ml DNaseI (Roche) in 0.1% BSA at 37°C, the tumor digest was filtered through 100 μm and 40 μm cell strainers to obtain single cell suspension. Cell were stained with antibodies listed in the Key Resources Table. Endothelial cells were selected as the CD45-GFP+CD31+ population.

Intestinal LECs were isolated from adult small intestine using cell sorting as described previously (Bernier-Latmani et al., 2015). The intestine was dissected and flushed with ice-cold PBS. Peyer's patches were removed and the intestine was cut into 1 cm pieces, which were put in a 10 mM EDTA solution with agitation at 37°C for 30 minutes to remove epithelial cells. The remaining tissue was then digested with Collagenase IV (3 mg/ml) in complete DMEM (GIBCO; ThermoFisher Scientific) containing CaCl$_2$ (2 mM) and 50 μg/ml DNase I, with constant stirring at 37°C for 20 minutes and washed with medium. The cell suspension was incubated with labeled antibodies listed in the Key Resources Table.

Skin endothelial cells were isolated from mouse ears as described previously (Vigl et al., 2011). Ears were separated into dorsal and ventral halves, cut into small pieces and digested in PBS containing 10 mg/mL of collagenase IV, for 13 minutes at 37°C while continuously rotating. This mix was passed through a 70 μm cell strainer placed in a 6 well plate and tissues were minced for 4 minutes. The plate with strainers was placed back at 37°C for 8 minutes. Cell suspension was placed on ice and passed another 4 times through a 40-μm cell strainer. Single-cell suspensions were stained with labeled antibodies listed in the Key Resources Table.

For isolation of lung endothelial cells Cnb1$^{\Delta bec}$ and Cnb1^{WT-GFP}, mice were injected i.v. with 5x10^5 B16F10-luc cells and i.p. with tamoxifen. 5 days after cancer cell injection, mice were anesthetized and perfused intracardially first with PBS and then with a digestion mix of 0.1% collagenase A (Roche) and 50 μg/ml DNaseI (Roche) in 0.1% BSA. Lungs were cut in pieces and incubated in digestion mix at 37°C for 45 minutes while continuously rotating at 150 rpm. Digested tissue was filtered through 100 μm and 40 μm cell strainers to obtain single cell suspension. 20 million cells were stained with antibodies listed in the Key Resources Table. All FACS sorting was performed on a BD FACSAria II (BD Bioscience).

Initially, we aimed to isolate lung BECs as Pdpn-CD31+GFP+ and lymphatic endothelial cells (LECs) as Pdpn+CD31+GFP- populations. Unexpectedly, we identified a third major Pdpn+CD31+GFP+ endothelial cell population, which we refer to here as BEC-2 (Figure S6E). qRT-PCR analysis of BEC, BEC-2 and LEC populations demonstrated that all of them expressed the pan-endothelial markers *CD31* and *VE-cadherin* (Figure S6F). BEC and BEC-2 were furthermore enriched in the blood endothelial-specific marker *Vegfr1* (Jurisic et al., 2012) (Figure S6G). In contrast lymphatic markers *Prox1*, *Vegfr3, Itga9, Nrp2* and *Pdpn* were highly expressed in LECs (Figure S6H). BEC-2 population showed no expression of lymphatic markers and more strikingly, although the cells were sorted based on the cell surface Pdpn+ expression, they did not contain *Pdpn* mRNA (Figure S6H). We thus propose that due to the particular organization of the lung capillary vasculature, the endothelial cells, located in close proximity of the podoplanin-expressing epithelial cells in order to allow gas exchange, acquire membrane of podoplanin positive cells during tissue digestion. The phenomena of cell membrane transfer was described before in subcapsular sinus macrophages (Gray et al., 2012). However, these cells that appear as Pdpn+ BECs (BEC-2) in our FACS analyses, will have not undergone any RNA transfer as they are devoid of *Pdpn* mRNA.

Immune cell analysis

For immune cell analysis we used Cnb1^{WT} and Cnb1$^{\Delta bec}$ animals injected with 5x10^5 B16F10-luc cells. 5 or 7 days after cancer cell injection, mice were anesthetized and perfused intracardially with PBS. Lungs were cut in pieces and digested in digestion mix (1mg/ml Collagenase type IV in DMEM) at 37°C for 45 minutes while continuously rotating at 150 rpm. Digested tissue was filtered through a 70 μm cell strainer to obtain single cell suspension. Cells were then stained for flow cytometry with anti-CD45-FITC, anti-CD3ε-e660, anti-CD8α-PerCP-Cy5.5, anti-CD4-A700, anti-CD44-Pe-Cy7, anti-CD62L-Pe and anti-B220-Texas Red (= lymphoid panel) or with anti-CD45-FITC, anti-CD11b-eFluor780, anti-Gr1-Alexa647, anti-Ly6C-PerCP-Cy5.5, anti-NK1.1-Pee, and anti-B220-Texas Red (= innate immune cell panel). Data were acquired on LSR II (BD Bioscience) and analyzed using FlowJo software (BD Bioscience). The following populations were analyzed: B cells (CD45$^+$B220$^+$), effector memory (CD62L$^-$CD44$^+$), central memory (CD62L$^+$CD44$^+$) and naive (CD62L$^+$CD44$^-$) CD4$^+$ and CD8$^+$ T cells, monocytes (Cd11b$^+$Ly6C$^+$), natural killer (Cd11b$^{+/-}$NK1.1$^+$) and neutrophils (Cd11b$^+$GR1^{hi}).

QUANTIFICATION AND STATISTICAL ANALYSIS

Image analysis

Retinas were imaged with an upright Zeiss Axio Imager Z1 using the tile scan and stitching function, for general overview pictures and to quantify the vessel branching and radial expansion. For vessel regression pictures were obtained with an inverted Zeiss LSM 880 confocal microscope. Retina analysis was performed with the Fiji software. Vessel regression analysis was performed by counting the collagen IV positive Icam2 negative structures and normalizing the counts to the total Icam2 positive area. Radial expansion was measured as the distance between the vascular front and the central optic nerve. Arterial and venous vessel branching was counted as the number of vessels branching off from the big central artery of vein visible per leaflet. Overall pericyte coverage was determined by measuring the total CD13 stained surface, further collagen IV positive, CD31 negative areas were selected and checked for CD13 positive staining to observe pericytes in empty sleeves. Proliferation of endothelial cells was measured in regions containing the vascular sprouting front by dividing the total number of ERG+ endothelial cell nuclei by the number of positive for ERG/EdU cells in 3–5 20x objective images. Apoptosis was quantified as the number of cleaved caspase-3+ events in CD31+ vessels divided by the total CD31 vessel area, and given as percentage of control.

For whole section analysis slides were imaged with the upright Zeiss Axio Imager Z1 using the tile scan and stitching function or either with the slide scanner Axio Scan.Z1. Confocal images were captured with an inverted Zeiss LSM 880 microscope. Area measurements were carried out using ImageJ software. Tumor vessel density was quantified as the CD31 area normalized to the total DAPI tumoral area. Empty sleeves in primary tumors were defined as avascular, CD31 negative regions, that were positive for collagen IV and 5 images per tumor were analyzed. For proliferation in lung metastasis, EdU was quantified as the total EdU positive area normalized to the whole lung section area. For the experiment using B16F10-GFP cells, EdU was normalized to the GFP positive metastatic area.

Statistical analysis

Pairwise comparisons were performed by two-tailed Student's t test. The MC38 3D spheroid growth *in vitro* and the mRNA expression of LEC, BEC and BEC-2 for their specific markers was analyzed by two-way ANOVA. Statistical details of experiments can be found in the figure legends.

Public dataset analysis

Affymetrix Human Genome U133 Plus 2.0 Array gene expression profiling dataset GSE49426 (Suehiro et al., 2014) from HUVECs treated with 50ng/ml VEGFA in the presence or absence of 1μM Cyclosporin A or HUVECs with adenovirally overexpressed caNFATc1 was downloaded and normalized with RMA (affy R package). Differential expression was computed with limma. In the absence of replicates, cutoffs based on log fold change (LFC) were decided to define differentially expressed genes: LFC > 0.5 defined upregulation by VEGFA in the absence of Cyclosporin A, LFC > 0.5 defined upregulation by VEGFA in the presence of

Cyclosporin A, LFC > 2.5 defined upregulation by caNFATc1. Genes induced by VEGFA without Cyclosporin A and induced by caNFATc1, but not induced by VEGFA in the presence of Cyclosporin A were selected and their expression is shown in a heatmap.

RNA-seq analysis

Mouse target transcript sequences were obtained from ENSEMBLE (GRCm38.p6), and the abundances of transcripts were quantified using Kallisto (0.44.0) with default parameters (Bray et al., 2016). Kallisto's transcript-level estimates were then summarized at the gene-level using tximport (1.8.0) from Bioconductor (Soneson et al., 2015). Raw and processed data are accessible from Gene Expression Omnibus (GEO) under accession number GSE117074.

Differential expression analysis was performed using DESeq2 (1.20.0) from Bioconductor (Love et al., 2014), with FDR < 0.05 and FoldChange > 2 as significance criteria. For gene set enrichment analysis (GSEA), human orthologs of mouse genes were obtained using biomaRt (2.36.1) (Durinck et al., 2005, 2009). GSEA enrichment scores were then computed using fgsea (1.6.0) from Bioconductor (Sergushichev, 2016), with gene sets obtained from MSigDB database (Liberzon et al., 2015; Subramanian et al., 2005), and DESeq2's LOG2FC as gene ranking metric.

We defined the Bmp2-treated mouse melanoma signature as the aggregated list of up- and downregulated genes obtained from DESeq2. To compare the enrichment of the Bmp2-treated mouse melanoma signature across human melanoma subtypes, processed gene expression data of metastatic skin cutaneous melanoma (SKCM) from TCGA was obtained from the cBioPortal (Cerami et al., 2012; Gao et al., 2013). Expression data was log transformed with offset = 1, and standardized across samples. Sample labels assigning each tumor to one of the four differentiation subtypes (melanocytic, transitory, neural crest-like, and undifferentiated) were directly obtained from (Tsoi et al., 2018). An enrichment score was then computed for the Bmp2-treated mouse melanoma signature per tumor, using a weighted sum of standardized expression values, where the weight was set to +1 for upregulated genes and −1 for downregulated genes.

DATA AND SOFTWARE AVAILABILITY

The RNA-seq data are deposited into Gene Expression Omnibus under accession number GEO: GSE111783.

Supplemental Information

Endothelial Calcineurin Signaling Restrains

Metastatic Outgrowth by Regulating Bmp2

Stefanie Hendrikx, Sanja Coso, Borja Prat-Luri, Laureline Wetterwald, Amélie Sabine, Claudio A. Franco, Sina Nassiri, Nadine Zangger, Holger Gerhardt, Mauro Delorenzi, and Tatiana V. Petrova
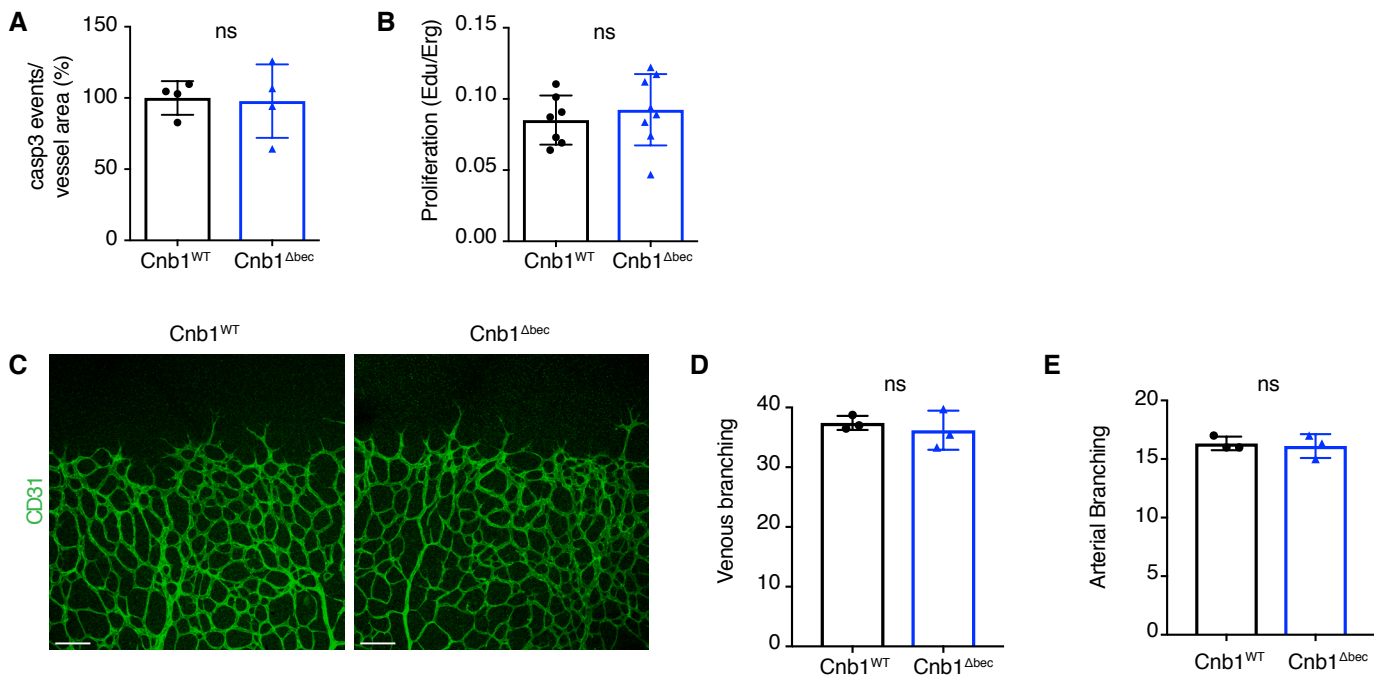
Figure S1, related to Figure 1. Endothelial calcineurin signaling does not affect sprouting angiogenesis or branching. (A) Loss of endothelial calcineurin does not affect retinal endothelial apoptosis. Quantification of caspase-3 positive cells normalized to the WT events per vascularized area (n = 4 Cnb1^{WT}; n = 4 Cnb1$^{\Delta bec}$). (B) Loss of endothelial calcineurin does not affect retinal endothelial cell proliferation. Quantification of number of proliferating endothelial cells as determined by staining for Edu and Erg (n = 7 Cnb1^{WT}; n = 8 Cnb1$^{\Delta bec}$). (C) Images of the angiogenic front of Cnb1^{WT} and Cnb1$^{\Delta bec}$ retinas. (D) Venous branching quantified as the number of vessels branching off from the vein is not affected in Cnb1$^{\Delta bec}$ retinas (n = 3 Cnb1^{WT}; n = 3 Cnb1$^{\Delta bec}$). (E) Arterial branching quantified as the number of vessels branching off from the artery is not affected in Cnb1$^{\Delta bec}$ retinas (n = 3 Cnb1^{WT}; n = 3 Cnb1$^{\Delta bec}$). ns = not significant, error bars represent mean ± SD, Two-tailed Student's t-test was performed on all data represented. Scale bar C = 100 μm.
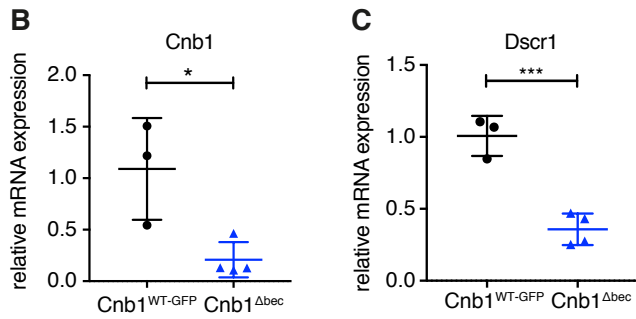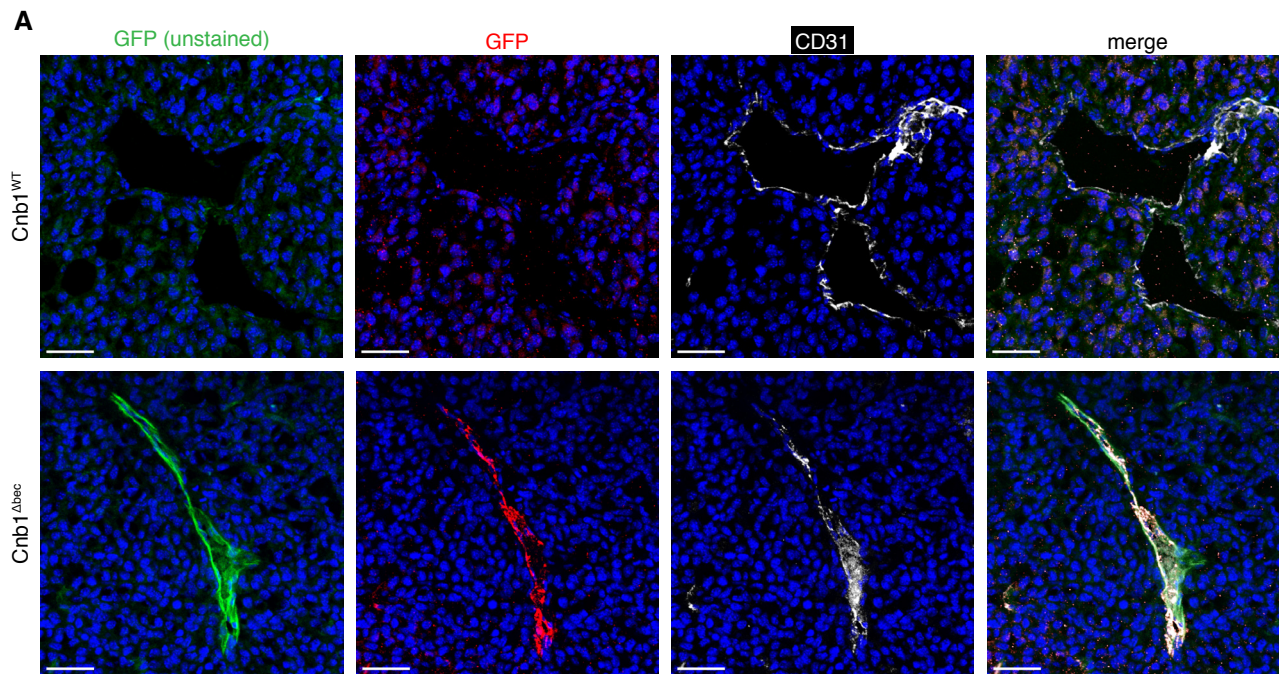
Figure S2, related to Figure 2. GFP expression and deletion efficiency of calcineurin in tumor endothelium. (A) Representative images showing EGFP and immunofluorescent staining for GFP and CD31 in Cnb1$^{\Delta bec}$ and Cnb1^{WT} tumors. As expected, GFP positive vessels in Cnb1$^{\Delta bec}$ tumors are absent in Cnb1^{WT} tumors. (B) Reduced expression of *Cnb1* in the Cnb1$^{\Delta bec}$ tumor endothelium (*p = 0.0173, n = 3 Cnb1^{WT}; n = 4 Cnb1$^{\Delta bec}$). (C) Reduced expression of *Dscr1* in the Cnb1$^{\Delta bec}$ tumor endothelium (***p = 0.0009, n = 3 Cnb1^{WT}; n = 4 Cnb1$^{\Delta bec}$). Error bars represent mean ± SD, Two-tailed Student's t-test was performed on all data represented. Scale bar: A = 100μm.

Figure S3, related to Figure 3. Endothelial calcineurin signaling restrains MC38 lung metastasis. (A) Representative images of MC38-GFP metastases in Cnb1^{WT} and Cnb1$^{\Delta bec}$ lungs. (B) Increased number of MC38-GFP colonies in Cnb1$^{\Delta bec}$ lungs, (*p = 0.0367; n = 6 Cnb1^{WT}; n = 7 Cnb1$^{\Delta bec}$). Error bars represent mean ± SD, Two-tailed Student's t-test was performed on data represented. Scale bar A = 1 mm.
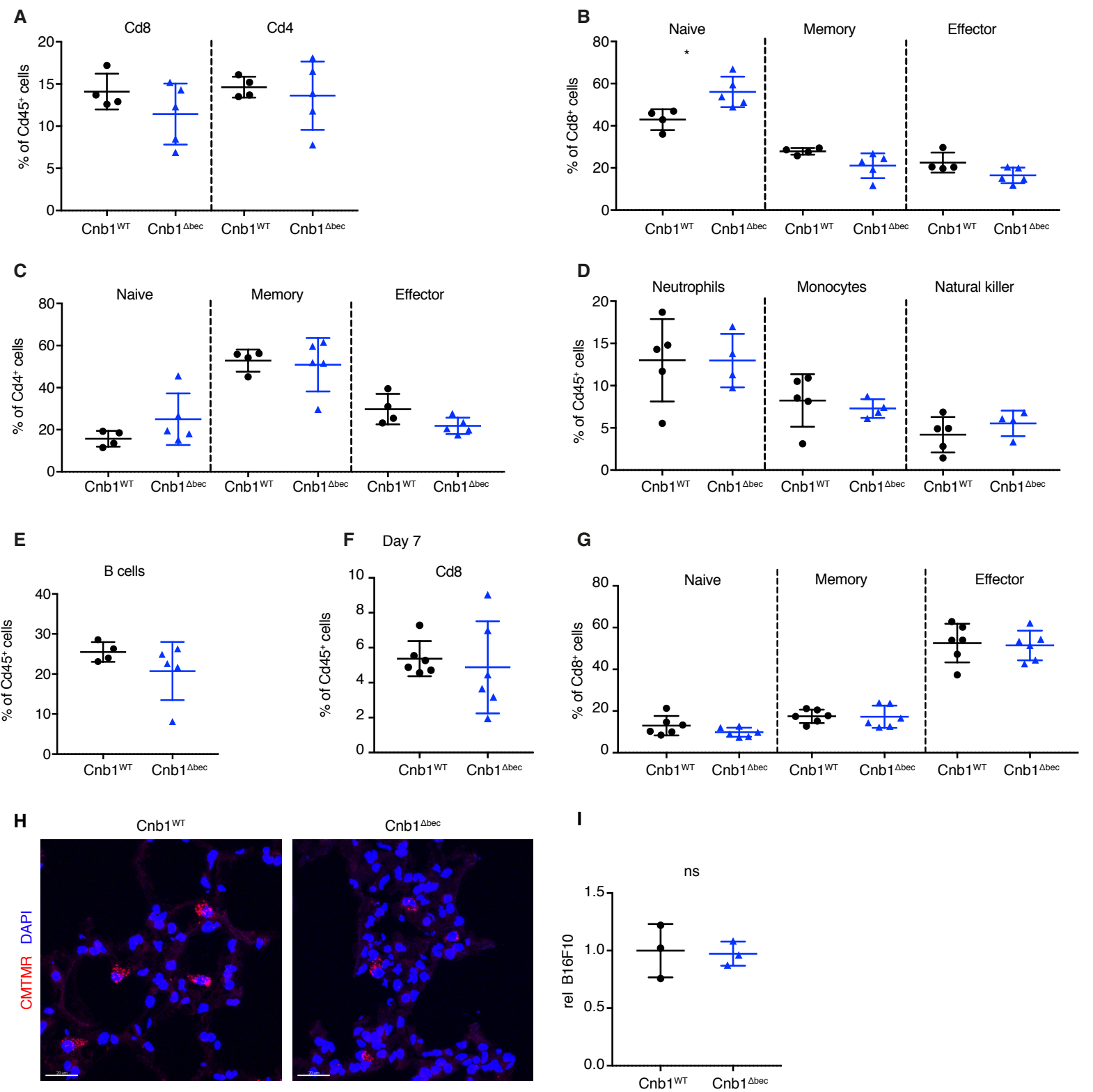
Figure S4, related to Figure 4. Immune cell populations in metastatic lungs is not affected by endothelial calcineurin deletion. (A) Comparable levels of Cd8+ and Cd4+ T cells in Cnb1^{WT} and Cnb1$^{\Delta bec}$ metastatic lungs at 5 days post i.v. injection (n = 4 Cnb1^{WT}; n = 5 Cnb1$^{\Delta bec}$). (B) Naïve Cd8 T cells were higher in Cnb1$^{\Delta bec}$ metastatic lungs, whereas no difference in central memory or effector memory Cd8 T cells was observed in Cnb1^{WT} and Cnb1$^{\Delta bec}$ metastatic lungs 5 days post i.v. injection (*p= 0.0174, n = 4 Cnb1^{WT}; n = 5 Cnb1$^{\Delta bec}$). (C) No difference in naïve, central memory or effector memory Cd4 T cells present in Cnb1^{WT} and Cnb1$^{\Delta bec}$ metastatic lungs 5 days post i.v. injection. (D) No difference was observed in neutrophils, monocytes and natural killer cells present in Cnb1^{WT} and Cnb1$^{\Delta bec}$ metastatic lungs 5 days post i.v. injection (n = 5 Cnb1^{WT}; n = 4 Cnb1$^{\Delta bec}$). (E) Comparable levels of B cells in Cnb1^{WT} and Cnb1$^{\Delta bec}$ metastatic lungs at 5 days post i.v. injection (n = 4 Cnb1^{WT}; n = 5 Cnb1$^{\Delta bec}$). (F) Comparable levels of Cd8+ T cells in Cnb1^{WT} and Cnb1$^{\Delta bec}$ metastatic lungs at 7 days post i.v. injection (n = 6 Cnb1^{WT}; n = 6 Cnb1$^{\Delta bec}$). (G) No difference in naïve, central memory or effector memory Cd8 T cells present in Cnb1^{WT} and Cnb1$^{\Delta bec}$ metastatic lungs 7 days post i.v. injection. (H) Representative images of Cnb1^{WT} and Cnb1$^{\Delta bec}$ lung sections 24h after intravenous injection of CMTMR-labeled B16F10 cells. (I) The number of B16F10 cells present in the lung 24h after i.v. injection is not affected in Cnb1$^{\Delta bec}$ mice (n = 3 per genotype). Error bars represent mean ± SD Two-tailed Student's t-test was performed for B. Scale bar H = 20µm. Error bars represent mean ± SD Two-tailed Student's t-test was performed on all data represented.
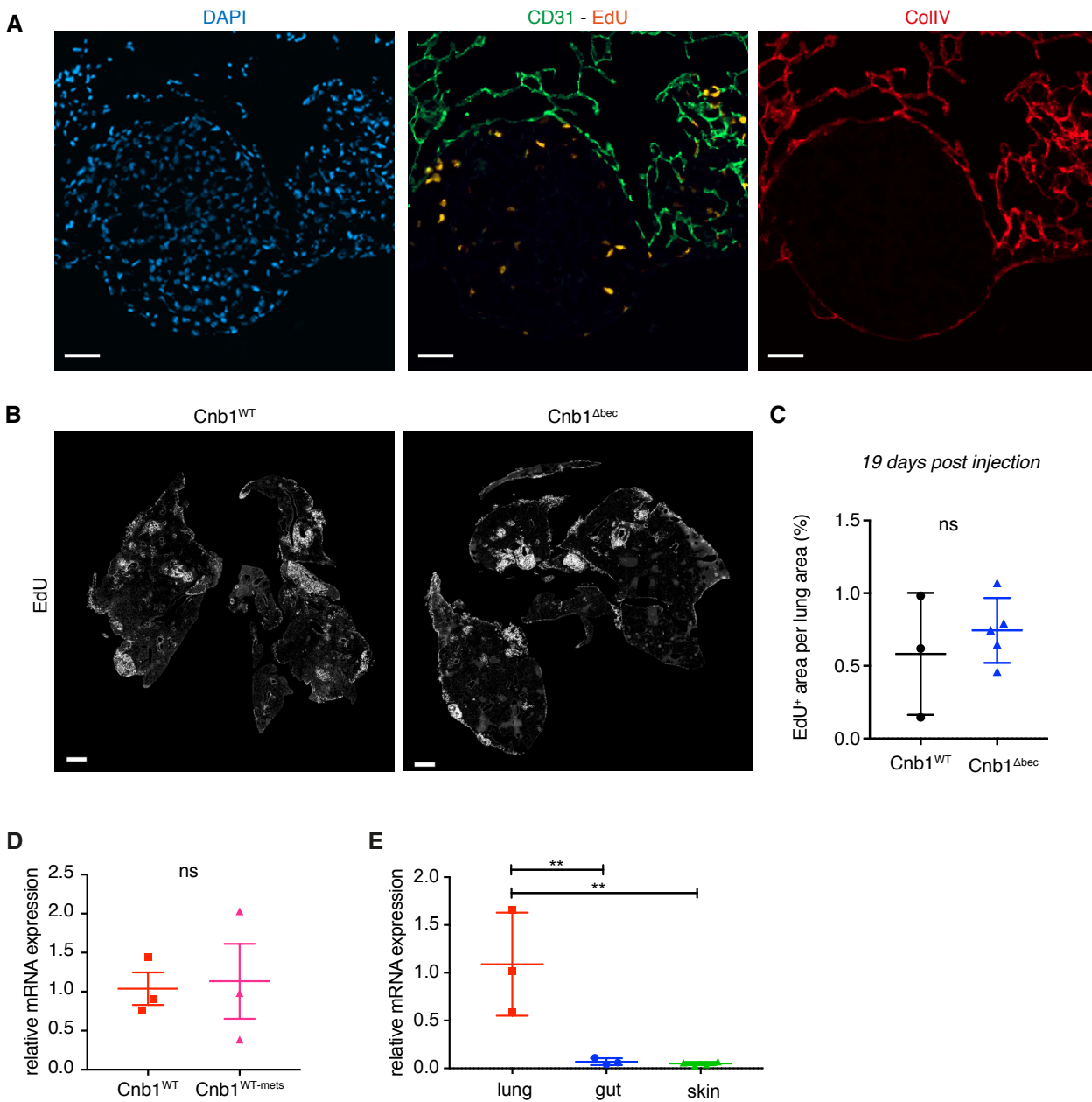
Figure S5, related to Figure 5. Vascular organization and NFAT activation in B16F10 lung metastasis. (A) Immunofluorescent staining for DAPI (blue), CD31 (green) EdU (orange) and collagen IV (red). Representative image of a B16F10 lung macrometastasis. Note mostly peritumoral CD31/collagen IV staining. EdU positive cells are mostly present at the metastatic border where B16F10 are in proximity of vessels. (B) Representative images of lung sections from Cnb1^{WT} and Cnb1$^{\Delta bec}$ mice 19 days post i.v. injection of B16F10, staining for EdU (white). (C) Macrometastases proliferation is not affected in Cnb1$^{\Delta bec}$ mice. The EdU positive area was quantified and normalized to the total lung area 19 days post i.v.injection of B16F10 cells (n = 3 Cnb1^{WT}; n = 5 Cnb1$^{\Delta bec}$). (D) *Dscr1* expression is not affected by the presence of metastasis (n = 3 Cnb1^{WT}; n = 3 Cnb1$^{WT\text{-mets}}$). (E) *Dscr1* expression is significantly higher in the lung blood endothelial cells compared to gut and skin endothelium (**$p < 0.01$, n = 3 lung; n = 3 gut; n = 4 skin). ns = non significant, error bars represent mean ± SD Two-tailed Student's t-test was performed on C and D, one-way ANOVA on E. Scale bar A = 50µm, B = 1mm.
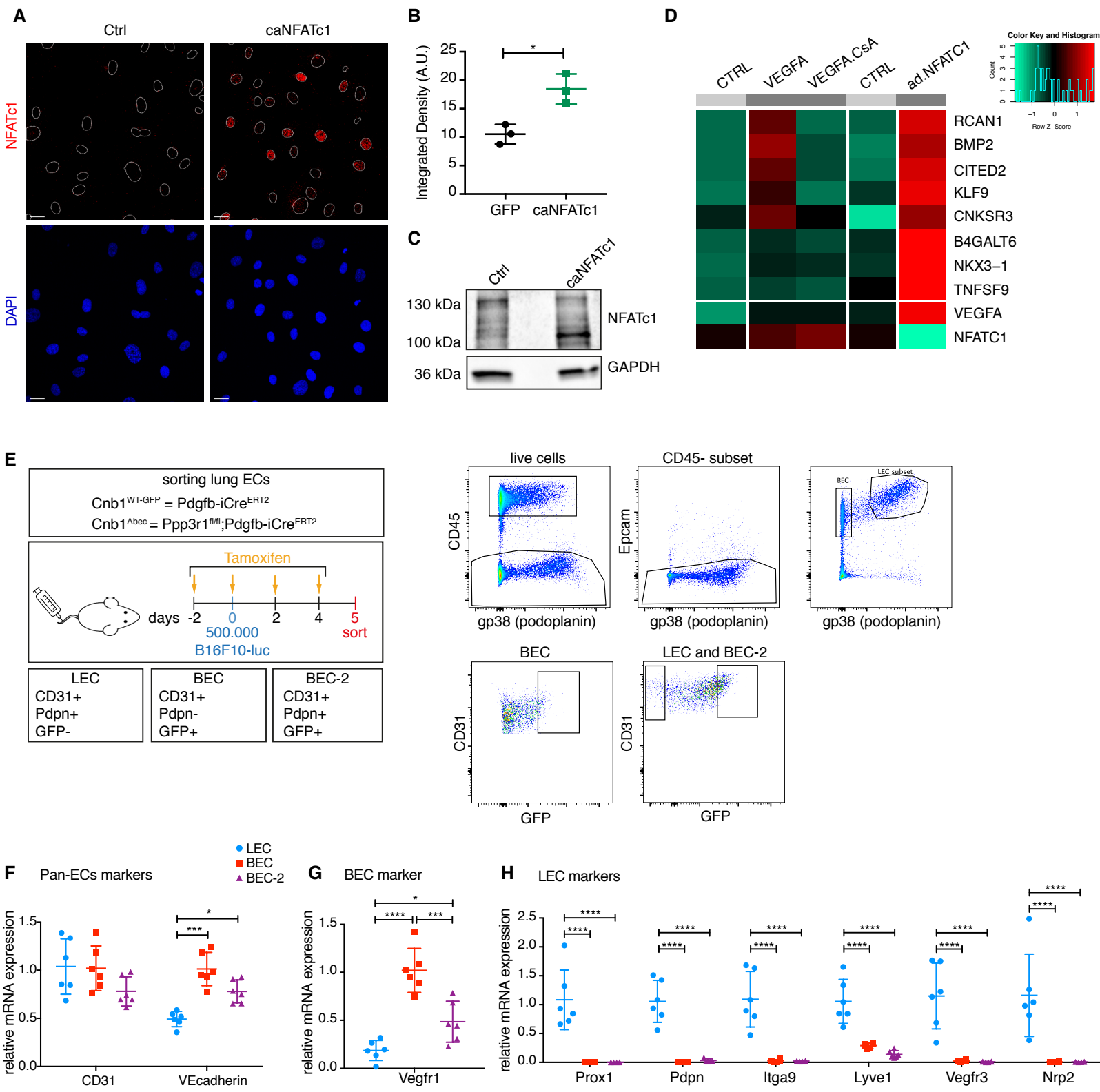
Figure S6, related to Figure 6. Identification of calcineurin/NFAT target genes and sorting of lung ECs. (A) Representative images of HUVECs transduced with GFP or caNFATc1 lentiviruses. Staining for NFATc1 (red) and DNA (blue) after 12h of serum starvation. (B) Quantification of nuclear NFATc1 staining in HUVECs transduced with caNFATc1 or GFP (*p = 0.0121, n = 3 GFP or caNFATc1). (C) A lower motility NFAT band is present in HUVECs transduced with caNFATc1 compared to control GFP. Western blot for the indicated proteins. (D) Heat map showing differentially expressed genes induced by VEGFA without Cyclosporin A and induced by caNFATc1, but not induced by VEGFA in the presence of Cyclosporin A. Microarray data from the publically available dataset GSE49426 was used (Suehiro et al., 2014). (E) Representative FACS plots and gating scheme for sorting endothelial cells from Cnb1^WT-GFP and Cnb1^Δbec lungs, showing BECs (CD31+, GFP+, Pdpn-), LECs (CD31+, GFP-, Pdpn+) and BEC-2 (CD31+, GFP+, Pdpn+). (F) Expression of pan-endothelial population markers *CD31* and *VEcadherin* is similar in BEC, LEC and BEC-2 (*p = 0.0323, ***p = 0.0001, n = 6). (G) Expression of blood endothelial marker *Vegfr1* is increased in BEC and BEC-2 compared to LEC (*p = 0.0397, ***p = 0.0006, **** p < 0.0001 n = 6). (H) LEC markers are expressed only by LEC population (**** p < 0.0001, n = 6). Error bars represent mean ± SD Two-tailed Student's t-test was performed on data represented in B and Two-way ANOVA was performed on F-H. Scale bar A = 20μm.
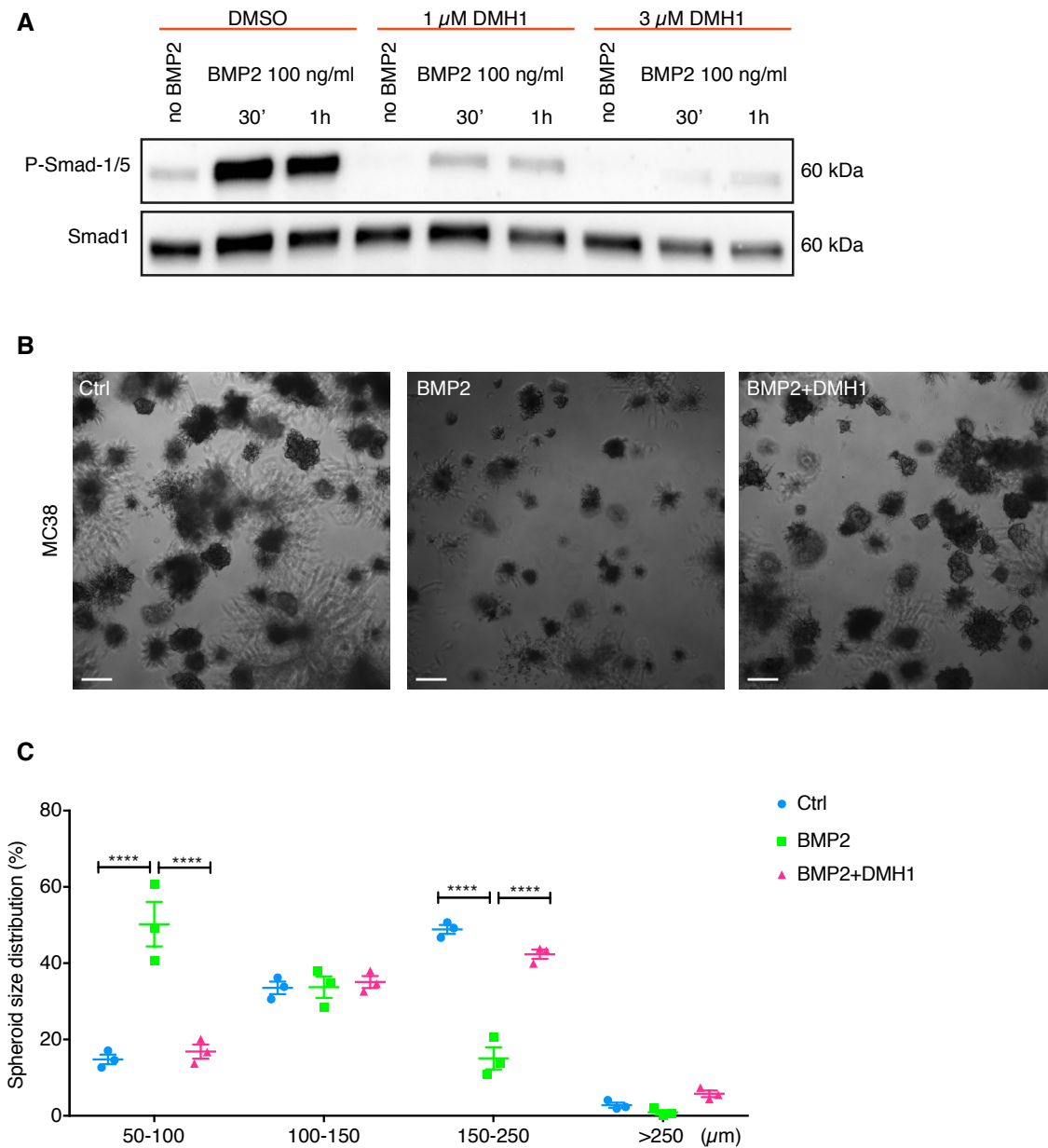
Figure S7, related to Figure 6. BMP2 inhibits MC38 tumor spheroids formation. (A) BMP2 induces phosphorylation of Smad-1/5 in MC38 cells. Cells were treated with 100 ng/ml BMP2 in the presence or absence of 1 μM and 3 μM DMH1 and lysates were prepared after 30 minutes and 1h. (B) Representative images of MC38 spheroids treated with Ctrl,100 ng/ml BMP2 or 3μM DMH1. (C) BMP2 treatment increases the number of small colonies (50-100 μm) and decreased the number of bigger colonies (150-250 μm) compared to control treatment, which can be rescued by DMH1 (***$p < 0.0001$, n = 3). Error bars represent mean ± SD Two-way ANOVA was performed for C. Scale bar: B = 100 μm.